5-2011

Numerical Simulations of Accretion Disks and Extrasolar Planets

Stefan Luketic
University of Nevada, Las Vegas

NUMERICAL SIMULATIONS OF ACCRETION DISKS AND EXTRASOLAR PLANETS

by

Stefan Luketic

Bachelor of Science
University of Zagreb
2002

Master of Science
University of Zagreb
2007

A dissertation submitted in partial fulfillment
of the requirements for the

Doctor of Philosophy in Physics
Department of Physics and Astronomy
College of Science

Graduate College
University of Nevada, Las Vegas
May 2011

UNLV
UNIVERSITY OF NEVADA LAS VEGAS

THE GRADUATE COLLEGE

We recommend the dissertation prepared under our supervision by

Stefan Luketic

entitled

Numerical Simulations of Accretion Disks and Extrasolar Planets

be accepted in partial fulfillment of the requirements for the degree of

Doctor of Philosophy in Physics

Daniel Proga, Committee Chair

Stephen Lepp, Committee Member

Michael Pravica, Committee Member

Rohan Dalpatadu, Graduate Faculty Representative

Ronald Smith, Ph. D., Vice President for Research and Graduate Studies
and Dean of the Graduate College

ABSTRACT

Numerical Simulations Of Accretion Disks And Extrasolar Planets

by

Stefan Luketic

Daniel Proga, PhD, Examination Committee Chair
Professor of Physics and Astronomy
University of Nevada, Las Vegas

We study mass outflows from astrophysical objects. Using numerical hydrodynamical simulations, we investigate outflows from accretion disks and exoplanets. In the first part of this dissertation, we present the results of Zeus 2D hydrodynamical simulations of the disk photosphere irradiated by strong X–rays that are produced in the innermost part of the disk of an accreting black hole. As expected, the irradiation heats the photosphere and drives a thermal wind. To apply our results to the well–studied X–ray transient source GRO J1655–40, we utilized the observed mass of its black hole and the observed properties of its X–ray radiation for our simulations. To compare our results with observations, we also computed transmitted X–ray spectra based on the wind solution. Our main finding is that the density of the fast–moving part of the wind is more than one order of magnitude lower than that inferred from the observations. Consequently, the model fails to predict spectra with line absorptions as strong and as blueshifted as those observed. However, despite the thermal wind being weak and Compton thin, the ratio between the mass–loss rate and the mass accretion rate is about seven. This high ratio is insensitive to the accretion luminosity, in the limit of lower luminosities. Most of the mass is lost from the disk between 0.07 and 0.2 of the Compton radius. We discovered that beyond this range the wind solution is self-similar. In particular, soon after it leaves the disk, the wind flows at a constant angle with respect to the disk. Overall, the thermal winds gen-

erated in our comprehensive simulations do not match the wind spectra observed in GRO J1655–40. This supports the conclusion of Miller et al. and Kallman et al. that the wind in GRO J1655–40, and possibly other X–ray transients, may be driven by magnetic processes. This in turn implies that the disk wind carries even more material than our simulations predict, and, as such, has a very significant impact on the accretion disk structure and dynamics. Motivated by the recent renaissance after the Kepler mission discoveries of about 500 new extrasolar planets, in the second part we analyze problems of the extrasolar planet irradiated by a star interacting with the wind coming from a parent star. This is a full 3D modeling performed using Athena 3D. We use the general model of a spherical object with a cosine distribution of temperature on the irradiated side and constant temperature on the opposite side. The thermal wind arises from the planet and interacts with the wind emanating from the star. We made some simplifications; the Coriolis force is included. We placed constraints on the mass loss from the planet, wind velocities, and dependencies on various parameters, such as: distance from the star, strength of the stars, wind, etc. We created a general model for studying outflows from diverse group of objects of various geometries.

TABLE OF CONTENTS

LIST OF FIGURES

ACKNOWLEDGMENTS

I would like to thank my mentor Daniel Proga, PhD, for all he did during last four and a half years of my graduate studies. I thank Tim Kallman, PhD, for the colaboration on our work on disk winds. I thank Timothy R. Waters for his comments on the manuscript and John Kilburg for all the computer support. I also thank Jim Stone for creating the codes we have been using. I thank Saju Varghese for help with visualisation software. I acknowledge support provided by the Chandra awards TM8-9004X and TM0-11010X issued by the Chandra X-Ray Observatory Center, which is operated by the Smithsonian Astrophysical Observatory for and on behalf of NASA under contract NAS 8-39073. Finally special thanks to all members of the committee: Stephen Lepp, PhD, Michael Pravica, PhD and Rohan Dalpatadu, PhD.

CHAPTER 1

INTRODUCTION

Since the early days of natural sciences and physics itself, there were two distinct approaches: theoretical and experimental. Of course those two were mutually dependent, but nevertheless differed in their methods and techniques. However, with the development of technology in modern society, another approach to scientific research arose: numerical simulation. In the early days, after acquiring a certain amount of experimental data, theory would try to generalize the results, and, after formulating a certain paradigm, would then attempt to extrapolate the solution outside of the margins where measurements were performed in order to provide predictions which would be later tested. Today, the numerical simulation approach serves as a bridge connecting the theoretical and experimental approaches. The numerical simulation approach recognizes theoretical physical laws and uses them to govern the physical processes in the virtual computer based space in order to provide the prediction.

This approach has been in use since the very beginning of the computer era. In its beginning days, the main limitation of the numerical simulation approach was the computational power of the machines. Although simple problems can be simulated to far better precision than any experiment available, just slightly more complex problems can often be limited in solution precision by that very same computational power. The reason for this is the enormous difference between lower and higher dimensional problems, and also by the amount of different physical laws one needs to incorporate into the simulation if the problem is not trivial and simple. One would be able to look at numerical simulation as just another form of theoretical solution, where instead of analytical solutions, one is numerically obtaining the solution for those same equations. Of course, there are many approximations, assumptions, and also "by hand" involvements in the process itself. Therefore it may, on the other hand, be called a numerical experiment. In this context, a very simple setup is closer to the

pure mathematical solving of the equations, while the more complex setup is closer to the numerical experiment. Thus, when considered as a link between theoretical and experimental approaches, the numerical simulation is a growing field with a very bright perspective.

From a physical point of view, the problems that we examine in this work entail the outflows from astrophysical objects with various geometries that can be explored and understood only via numerical simulations, or more specifically, numerically solving, time–dependent differential equations. The attempts to attack similar systems were numerous in the past. Before the current computational power reached the level for multidimensional simulations, due to the progress of the technological development, much research was done on one–dimensional, spherically symmetric systems. Such numerical experiments could not reveal the secrets of the systems which are inherently not spherically–symmetric, such as accretion disks. Although there are systems which have a big enough degree of spherical symmetry, in those rare cases, one–dimensional simulations can indeed provide some insight into the system. Those, and some other more–than–one–dimensional systems, did include most of the relevant physics in the analysis. To analyze accretion disks, one needs at least a two–dimensional simulation, with the rotation included (sometimes called 2.5 dimensional because of all third dimension physical quantities that are included but assumed to be perfectly axis symmetrical).

Historical Background

As both parts of this work are based upon numerical simulations, we start with a historical overview from the two or higher dimensional simulations performed in the past. We will discuss only those of relevance for this work. In the case of the accretion disk simulations (though not the very first, but certainly one of the most significant) early 2D numerical simulations were performed by Woods et al. (1996). [1] The

relevance of this work is that it provides, for the first time, the two–dimensional structure of a thermally driven wind from the accretion disk heated by X–rays from the central source. The geometrical structure of the wind cannot be explored by one–dimensional simulations performed earlier. Calculations were time–dependent and axis–symmetric, hydrodynamic simulations, using local adaptive mesh refinement of thermally–driven, rotating winds from X-ray irradiated accretion disks. This model relies on the previous analytic predictions of Begelman et al. (1883) [2] for Compton–heated winds, including non–Compton processes, such as photoionization heating and line cooling that are typical of X-ray heated winds. The Woods' simulation improved the analytical prediction of Begelman et al. (1883) [2] , provided a new expression for mass–loss rate, and gave a modified view of the solution topology. Also, for our research, of importance is Shields' et al. (1986) [3] work on accretion disk instabilities and oscillations. More recently, similar numerical simulations of accretion disks were done by Proga et al. (PK02, PSK00) [4] [5] using the Zeus 2D code developed by Stone et al. (1992). [6] The Zeus 2D code and the related works of importance for our research will be described in more detail in subsequent chapters. The same authors later created another code, the Athena 3D code, which we used to perform the latest numerical experiments, which will also be described in more detail. The codes are dealing with magnetohydrodynamical processes, and recently relativistic equations were incorporated into Athena. The Zeus2D is a 2.5D code, with three different built–in coordinate systems. The polar axis symmetric system is very suitable for exploring accretion disk geometries, which together with its ability to have logarithmic radial and angular resolution is its main advantage over the Athena.

Athena is a 3D code which, being newer, has many advantages over Zeus. Its main drawbacks may be the Cartesian coordinate system and linear grid scaling. For the investigation of non–axis symmetric effects on extrasolar planets to make 3D simulations, it was necessary to use. We had an option to continue with the Zeus code

in one of its three dimensional versions, such as Zeus 3D or Zeus MP, but, although they are newer codes developed after Zeus 2D, they still use the same algorithms, and it seems the development on Zeus is slowly ceasing. In the meantime, the same authors are focusing on the development of the Athena code, and are constantly adding more physics and refining the old versions. Also, other than the brighter future that Athena has, the difference and superiority over the Zeus is another important factor. Athena has many more superior built–in algorithms for solving physical equations, which is explained in full detail in the chapter on extrasolar planets. Also, Athena is capable of dealing with a much larger class of problems, and its structure is more open for adding extra physics when needed.

Problems Investigated

The first part of our work is focused on the specific system of an X–ray binary system, specifically GRO J1655–40. This system has an accretion disk and wind arising from the disk (Miller et al. 2006) [7] . However, details about the mechanism driving the wind are a subject of a discussion. We provided the numerical results of the simulation, which clearly discard some of the suggested mechanisms. This particular discussion was focused on whether wind is driven thermally (Netzer 2006) [9] or by magnetic fields (Miller et al. 2008) [10] , where all sides were excluding radiation driving as a possibility because of the specific geometrical distances within the system. In our simulation, we have shown strong evidence that the thermal mechanism itself cannot be sufficient to drive the wind of observed strength, leaving the only possible mechanism for wind generation to be the magnetic field.

The second part of our research investigates the wind arising from the extrasolar planets. This part of our work does not stress any specific system but is, in this phase of development, a generalized extrasolar planet system with the wind, in the dimensionless units. Because of the vast amount of extrasolar planets being discovered

while this work is in progress, our results will be applicable to many observed cases.

One way of observing exoplanet atmospheres is by taking an image of the exoplanet. This method is direct imaging of planets, and it is currently limited to big, bright, young, or massive planets, located far from their stars. Planets like those in the solar system, and other small exoplanets, are not observable via direct imaging with current technology.

Astrophysics of extrasolar planets is the field that is going through a revolution. The recent Kepler mission revealed hundreds of new candidates for extrasolar planets and increased, until recently, the very small sample of observed extrasolar planets, by an order of magnitude in the total number of detections (Schneider 2011) [11] . The majority of the planets are detected by the method of radial velocity, or astrometry. As a planet orbits a star, the star also moves in its own very small elliptical orbit around the system's center of mass. Variations in the star's radial velocity can be detected by displacements in the star's spectral lines, due to the Doppler effect. About 400 planets have been found using this method. The second most successful method counts around 100 planets and is the method of transiting planets. If a planet crosses, or transits, in front of its parent star's disk, then the observed brightness of the star drops by a small amount. The amount by which the brightness of the star dims depends on its size and on the size of the planet in transit, among other factors. Other methods of detection, all together, count about thirty detections. In the method of micro lensing, the gravitational field of a star acts like a lens, magnifying the light of a distant background star. Planets orbiting the lensing star can cause detectable anomalies in the magnification as it varies over time. The method of astrometry precisely measures a star's position in the sky and observes the changes in that position over time. The motion of a star, due to the gravitational influence of a planet, may be observable. Extoplanet can also be detected by timing. If planets orbit the pulsar, they will cause slight anomalies in the timing of its observed

radio pulses, or if a planet has a large orbit that carries it around both members of an eclipsing double star system, then the planet can be detected through small variations in the timing of the stars' eclipses of each other.

Most extrasolar planet candidates were found using ground–based telescopes. However, many of the methods described above are more effective with space–based telescopes that avoid atmospheric haze and turbulence. The future of exoplanetology is bright, since we already know that at least 30% of sequence stars have one, or several, super-Earth companions (Mayor 2008) [12] . It is likely that there will be two generations of space missions for the direct characterization of exoplanets in the next 15–20 years: a first generation with a 1.5-2m class chronograph, suited for giant planets and nearby super–Earths (e. g. Schneider et al. 2009) [13] , and a second generation, consisting of an interferometer (Cockel et al. 2009, Lawson et al. 2009) [14] [15] , an external occulter (Glassman et al 2009) [16] , a large 8m class coronagraph (Shaklan and Levine 2008) [17] , a Fresnel Interferometric Imager (Koechlin et al 2009) [18] or a 20m segmented coronagraph (Lillie et al. 2001) [19] . A coronograph is a telescopic attachment designed to block out the direct light from a star so that nearby objects, which otherwise would be hidden in the star's bright glare, can be detected.

Hot Jupiters are the type of exoplanet currently easiest to study. Detections of molecular spectral features, observation of day–night temperature gradients, and constraints on vertical atmospheric structure are being made. Atmospheres of giant planets, far from their host stars, are also being observed with direct imaging. The biggest exoplanet goal is to answer the question of the existence of extraterrestrial life via detection of atmospheric signatures of primitive forms of life.

The existence and discovery of a large population of planets has enabled observations of exoplanet atmospheres, using a technique very different from direct imaging. orbiting very close to their host stars. The hot Jupiters, hot Neptunes, and hot super

Earths have up to about four–day orbits and semi–major axes less than 0.05 AU. The hot Jupiters are heated by their parent stars to temperatures of 1000 to 2000 K, making their IR brightness on the order of 1/1000, with respect to their parent stars. What also enabled observations of exoplanet atmospheres, is that part of transiting exoplanets at some point on their orbit align their parent star. The closer the planet is to the parent star, the higher its probability to transit. The existence of short period planets enabled the discovery of many transiting exoplanets. It is the special transit configuration that enables the planet atmosphere to be observed without imaging the planet (Seager & Deming, 2010) [20] .

In our simulations, we put constraints on physical quantities, such as the total mass–loss rate of the planet, or velocity of the wind, and we provide some insight into the geometry of the wind itself. The simulations are done in a dimensionless system, and, due to the time limitations, did not explore the amount of parameter space we initially intended. However, they provide interesting insights.

We used the Zeus code for the first part of this research, exploring thermal winds from the accretion disks, while using the Athena code for the second part, where we explored thermal winds from the extrasolar planets. Although this research was done on apparently different systems, the first part on X–ray binaries and the second part on the planet irradiated by the star, the essence of the processes we explored is the same. In both cases, there is a surface irradiated by an external object, and although geometries of those simulations differ, the resulting processes can be regarded as one process with different boundary conditions, regardless of how different the actual physical objects seem to be. Therefore, a similar treatment is used to obtain the answer about the mechanism driving the winds from the accretion disk, and to put constraints on the mass–loss rate, as in the case of the extrasolar planet winds.

Precise theoretical models of winds from highly irradiated extrasolar planets are of interest to interpret the observations and to place firmer constraints on the mass–

loss rates. If these rates are higher than the lower limits on mass losses observed on some of detected planets, then some of those planets over their lifetimes will lose a significant enough percentage of their total mass to alter their structure and evolution (Hubbard et al. 2007; Lecavelier des Etangs 2007) [21] [22] .

CHAPTER 2

DISK WINDS

Brief Description of the Zeus 2D Code

Zeus 2D (developed by Stone et al. 1992) [6] is a numerical code for the simulation of fluid dynamical flows in astrophysics, including a self–consistent treatment of the effects of magnetic field and radiation transfer. The code has algorithms for hydrodynamics (HD), magnetohydrodynamics (MHD), and radiation hydrodynamics (RHD). This code uses simple, well–developed Eulerian HD algorithms, based on the method of finite differences implemented in a covariant formalism. The finite differencing method is attractive for many reasons: it is robust, easily modified, and extended with new algorithms. The finite difference equations are written in covariant form on an arbitrary moving orthogonal grid, which enables the accurate simulation of different flow geometries under translations and changes of scale. Time evolution of the system is governed by the equations conserving macroscopic properties: conservation of mass, momentum, and energy equation.

$$\frac{D\rho}{Dt} + \rho\nabla \cdot \mathbf{v} = 0, \tag{2.1}$$

$$\rho\frac{D\mathbf{v}}{Dt} = -\nabla P - \rho\nabla\Phi, \tag{2.2}$$

$$\rho\frac{D}{Dt}\left(\frac{e}{\rho}\right) = -p\nabla \cdot \mathbf{v}. \tag{2.3}$$

The dependent variables are the mass density ρ, the velocity $\mathbf{v}$ and the internal energy density e. Φ is gravitational potential and $\frac{D}{Dt}$ is the Lagrangian or comoving derivative:

$$\frac{D}{Dt} \equiv \frac{\partial}{\partial t} + \mathbf{v} \cdot \nabla. \tag{2.4}$$

The fluid equations are closed with an equation of state, which gives the gass pressure p as a function of the mass and internal energy density (or equivalently the mass density and temperature), and Poisson equation, which determines the gravitational potential Φ:

$$\nabla^2 \Phi = 4\pi G\rho. \tag{2.5}$$

The fluid equations are simply statements of macroscopic conservation laws. In Zeus the equation for internal energy is used, rather than the conservation law, for the total energy for highly supersonic flows. For the purposes of the Zeus code, it is sufficient to note that for many astrophysical gas dynamic problems one can show that inter particle collisions are frequent enough to allow one to use the continuum (macroscopic) description of the system given by above equations. Still, there are many microphysical processes that are not considered by the code, like the heat conduction. The equations of HD are a set of coupled hyperbolic partial differential equations. Zeus 2D solves the fluid equations using the method of the finite differences with a time explicit multistep (operator split) solution procedure. An operator split method breaks the solution of PDEs into parts, with each part representing a single term in the equations. Each part is evaluated successively, using the results from the update preceding it.

Explicit multi step schemes are generally more accurate than a single step that simply extrapolates forward in time on the basis of old data. Examples include the Lagrange–Remap formalism in the Prediction by Partial Matching algorithm [23], Flux Corrected Transport [24], Lax–Wendorff [25], and other predictor–corrector algorithms. Zeus solves above fluid equations in two steps, called the source and trans-

port steps. In the source step it accelerates the fluid velocity due to pressure, gravity and Lorentz forces, and performs pressure work, on the gas internal energy using finite–difference approximations. This calculation has the artificial viscous tensor Q included to treat the shock waves. Zeus implements several choices for Q which have advantages in different applications. In the transport step, fluid and magnetic flux are transported through the computational mesh conservatively using finite–difference approximations.

In the source step, there are three substeps. In the first step, the velocities are updated due to pressure gradients, gravitational forces, and coordinate curvature terms. In the second step, the partially updated velocities are used to add the artificial viscous stresses and dissipation. In the third step, the compressional heating term is applied to the gas energy. Only a few of the equations will be shown below, and are for the purpose of the illustration only. The first step contains physical accelerations and curvature terms, subscript n denotes the quantities at the start of source step, while a, b, and c denote the partially updated quantities from each of above three substeps (i and j are denoting grid position). Also notation used is: $v_1(x_1, x_2) \rightarrow v1(x1a_i, x2b_j) = v1_{i,j}$.

$$\left(v1_{i,j}^{n+a} - v1_{i,j}^{n}\right)/\Delta t = -\frac{p1_{i,j}^{n} - p1_{i-1,j}^{n}}{dx1b_i(d1_{i,j}^{n} + d1_{i-1,j}^{n})/2} - \frac{\Phi_{i,j}^{n} - \Phi_{i-1,j}^{n}}{dx1b_i} +$$

$$\frac{[(v2_{i,j}^{n} + v2_{i,j+1}^{n} + v2_{i-1,j}^{n} + v2_{i-1,j+1}^{n})/4]^2}{g2a_i}\left(\frac{\partial g2a_i}{\partial x_i}\right) + \frac{[(v3_{i,j}^{n} + v3_{i-1,j}^{n})/2]^2}{g31a_i}\left(\frac{\partial g31a_i}{\partial x_i}\right)$$

The second step deals with the artificial viscous acceleration and implements both a von Neumann and Ritchmyer–like artificial viscosity and a tensor artificial viscosity to treat shocks (Neumann & Richtmyer, 1950) [26] . The former is simpler and works

well in most circumstances. In the third step the source step is completed by adding the compressional heating term. In case of an ideal gas equation of state, an implicit update involving the time centered pressure is used to improve energy conservation.

In the transport step, the finite–difference approximations to the integral advection equations are solved. A finite–difference approximation to these equations, which is second order–accurate in space and time, is used. The flux in one direction is the same on the surface entering the cell and leaving the cell. Exact conservation of the flux variables can be acheived by computing the fluxes for every interface on the grid at once, and then using the same flux to update adjacent zones. Integrating over the ehtire computational domain, by summing over all zones, causes the flux to cancel in pairs, thus, except for the flux across the domain boundaries, the total flux is conserved.

The control of the time step is determined in a way that it satisfies the Courant–Friedrich–Lewy stability and accuracy condition:

$$\Delta t \leq min(\Delta x)/(|u| + C_a), \tag{2.6}$$

where u is the local fluid velocity, $C_a$is the local adiabatic speed of sound and the minimum is taken over all grid zones. The content of this section dealing with the numerical description of the Zeus code is mainly taken from Norman & Stone, 1992 [27] .

Disk Winds

Our simulations on the accretion disk of J1655–40 do not contain physics of the general theory of relativity (GTR). The zone where the wind is arising is not affected by GTR because of its distance from the central massive object which is bending the space around itself. Accretion is by far the most efficient mechanism for converting

mass into energy, and the details of that mechanism are not fully understood [28] . This mechanism is powering the whole system, and has an essential role in the process, but the radii where it occurs are much smaller than the radii from which the wind is emerging. In our simulations, we focus only on the region beyond the reach of GTR processes and on radii much higher than those where most of the energy is released by the central powering engine. We do not include magnetic processes. Also we do not deal with any microphysical processes directly, until we obtain the final steady state of the simulation, and only then the spectral analysis is done. The details of the geometry of the central heating engine are also simplified, by considering it to be a central source located a certain height above the disk on the axis. This is physically approved by associating it with a hot corona. The electric radiation pressure, as well as line radiation pressure, are neglected. Self–gravity is not included. In terms of heating, the model is dealing with the compton heating, photoionization, and shocks. Figure 1 is an artist rendering of an accretion disk.

Prior to proceeding with the work on the wind from the accretion disk, as a part of training and also for purposes of testing the Zeus code, we reproduced all simulations from the Font et al. (2004) [29] paper, and re–did most of the graphs in more detail than in the original paper. Once we acquired the full information on the code, after we tested it in detail comparing it to theoretical solutions of some simple problems, and after we obtained insight into the impact of the resolution limitations, we proceeded with the following research, which is presented in its entirety below [30] :

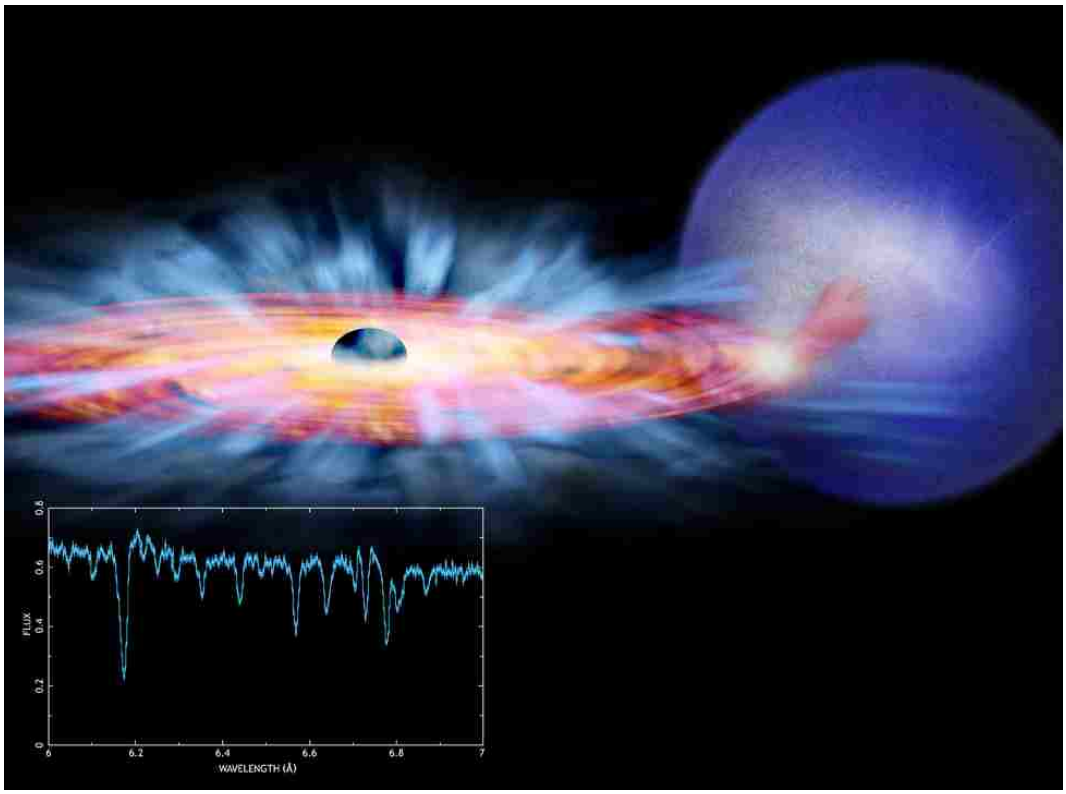

Figure 1 Accretion Disk (Artist Rendering), http://chandra.harvard.edu/photo/

On the Properties of Thermal Disk Winds in X-Ray Transient Sources: a Case Study of GRO J1655–40 [30] .

S. Luketic[1], D. Proga[1], T.R. Kallman[2], J.C. Raymond[3], and J.M. Miller[4]

[1] Department of Physics, University of Nevada, Las Vegas, NV 89154, stefan@physics.unlv.edu, dproga@physics.unlv.edu

[2] NASA, Goddard Space Flight Center, Laboratory for High Energy Astrophysics, Code 662, Greenbelt, MD 20771

[3] Harvard-Smithsonian Center for Astrophysics, 60 Garden St., Cambridge, MA 02138

[4] Department of Astronomy, University of Michigan, 500 Church Street, Ann Arbor, MI 48109

Abstract

We present the results of hydrodynamical simulations of the disk photosphere irradiated by strong X–rays produced in the innermost part of the disk of an accreting black hole. As expected, the irradiation heats the photosphere and drives a thermal wind. To apply our results to the well–studied X–ray transient source GRO J1655–40, we adopted the observed mass of its black hole, and the observed properties of its X–ray radiation. To compare the results with the observations, we also computed transmitted X–ray spectra, based on the wind solution. Our main finding is: the density of the fast–moving part of the wind is more than one order of magnitude lower than that inferred from the observations. Consequently, the model fails to predict spectra with line absorption as strong and as blueshifted as those observed. However, despite the thermal wind being weak and Compton thin, the ratio between the mass–loss rate and the mass–accretion rate is about seven. This high ratio is insensitive to the accretion luminosity, in the limit of lower luminosities. Most of the

mass is lost from the disk between 0.07 and 0.2 of the Compton radius. We discovered that beyond this range the wind solution is self–similar. In particular, soon after it leaves the disk, the wind flows at a constant angle with respect to the disk. Overall, the thermal winds generated in our comprehensive simulations do not match the wind spectra observed in GRO J1655–40. This supports the conclusion of Miller et al. and Kallman et al. that the wind in GRO J1655–40, and possibly other X-ray transients, may be driven by magnetic processes. This in turn implies that the disk wind carries even more material than our simulations predicted and, as such, has a very significant impact on the accretion disk structure and dynamics.

Paper Introduction

Most X–ray sources are powered by disk accretion onto compact objects. Therefore a main challenge for X–ray astronomy is to understand the mechanisms that enable this process. High quality and high spectral–resolution observations obtained with *Chandra*, *XMM-Newton*, and *Suzaku* allow us to study disk accretion and related outflows better than ever before. These observations are especially revealing if taken of relatively bright, well studied objects, such as X-ray transient sources, with GRO J1655–40 being a very fine example.

Many properties of GRO J1655–40 are well constrained. For example, GRO J1655–40 is a black hole binary at a distance of 3.2 kpc containing a black hole with a mass of 7.0 $M_{\odot}$ that accretes from an F3 IV–F6 IV star with a mass of 2.3 $M_{\odot}$ in a 2.6-day orbit. The inner disk is viewed at an inclination of 67° – 85° (nearly edge-on; Orosz & Bailyn 1997) [32] . When GRO J1655–40 is in an X-ray–bright phase, it is possible to obtain with *Chandra* high signal-to-noise spectra as shown by Miller et al. (2006a; M06 hereafter) [7] . In fact, the quality of the spectra obtained by M06 [7] is good enough to reveal many absorption lines significant at the 5 σ level of confidence, or higher. Over 70 of these lines can be identified as resonance lines,

from over 32 charge states. This is in sharp contrast to high resolution spectra of other systems (see below) and of GRO J1655–40 in other spectral states, when only the absorption lines of Fe XXV and XXVI are detected (e.g., Miller et al. 2006b; Kubota et al. 2007; Miller et al. 2008; Neilsen & Lee 2009) [31] [33] [10] [34] .

It is hoped that such high quality spectroscopy can provide new and surprising results. Indeed, absorption lines discovered by M06 are blueshifted, and likely produced in a disk wind, making GRO J1655–40 the best case for an X–ray binary, with an X–ray absorbing disk wind. But there are also other cases. For example, *Chandra* and *RTXE* spectroscopy of the microquasar H 1743−322 reveals blueshifted absorption lines that are likely formed in a disk wind (Miller et al. 2006b) [31] . Another example is the X–ray transient 4U 1630–472. Outburst spectra of this source obtained with *Susaku*, show iron absorption lines indicative of a disk wind (Kubota et al. 2007) [33] . More recently, Neilsen & Lee (2009) [34] found an X–ray absorbing disk wind in the microquasar GRS 1915+105. In addition, there is an outflowing X–ray absorber in Circinus X–1, which could either be a disk wind or a wind from a massive companion star (Schulz & Brandt 2002) [35] .

The disk wind discovered in GRO J1655–40 gives us a good testbed for constraining wind properties, using X–ray observations. For example, by fitting to observations 1–dimensional (1–D) models, M06 [7] and Miller et al. (2008) [10] put strict limits on the ionization balance in the wind. This was facilitated by the fact that some of the detected lines provide a density diagnostic. The main results from the fitting yielded the following parameters: number density n between 5×10^{13} cm^{-3} and 2×10^{14} cm^{-3}, column density $N_{\rm H} = 7.4 \times 10^{21}$ cm^{-2}, distance from the central object to the point of emerging of the strong wind 4.8×10^{8} cm and velocity $v_{\rm r} = 500$ km s^{-1}. The lines show blueshifts in the 300–1600 km s^{-1} range.

Using these wind properties, together with the observed wind speed and the system luminosity, M06 [7] concluded that the inferred wind location is well within the

Compton radius (the radius where the gravitational and thermal pressures are equal), defined by:

$$R_{\rm IC} = \frac{GM_{\rm BH} m_{\rm p} \mu}{kT_{\rm IC}}, \tag{2.7}$$

where $M_{\rm BH}$ is the mass of the black hole, μ is the mean molecular weight, $m_{\rm p}$ is the proton mass, and $T_{\rm IC}$ is the Compton temperature (for $M_{\rm BH} = 7\,{\rm M}_{\odot}$, $\mu = 0.6$, and $T_{\rm IC} = 1.4 \times 10^7$ K, the Compton radius is $R_{\rm IC} = 4.8 \times 10^{11}$ cm). This wind location is then inconsistent with an outflow being driven by thermal expansion, even though weak flows are possible at ~ 0.1 of the Compton radius, as found by Woods et al. (1996; see also Proga & Kallman 2002, hereafter PK02). [1] [4] On the other hand, the wind cannot be driven by radiation pressure in this system because the luminosity, L_*, relative to the Eddington limit, $L/L_{\rm Edd} = 0.03$, is too low (e.g., PK02) [4] . Therefore, by a process of elimination, M06 [7] concluded that the only plausible mechanism that could drive the wind is magnetic processes. MO6 [7] also concluded that disk accretion itself is driven by magnetic fields.

Although magnetic forces can drive a disk wind (e.g., Blandford & Payne 1982) [36] and magnetic fields are a very important ingredient of accretion disks (Balbus & Hawley 1998) [37] , M06's [7] arguments for magnetic driving are indirect (see also Proga 2006) [38] . Ideally, one should demonstrate that magnetic forces can drive a disk wind capable of reproducing the observed spectra. However, that is a relatively challenging task, and instead one could try to verify first whether thermal driving is indeed unsatisfactory. This is a very relevant question especially in light of the work done by Netzer (2006; N06 hereafter) [9] , who argued that it is possible to produce a simple thermally driven wind that is consistent with the observed properties of GRO J1655–40.

One can argue for or against thermal driving by comparing the escape velocity and the isothermal sound speed at the Compton temperature (equivalently, one can

compare the wind launching radius, $R_{\rm l}$ with, $R_{\rm IC}$ as M06 [7] did). To use this basic physical argument, one needs to estimate the wind temperature and $R_{\rm l}$. The former can be constrained relatively well for the Compton heated gas, whereas the latter is much more difficult to constrain. In fact, the controversy about the role of thermal driving has its origin in two different estimates for $R_{\rm l}$: M06 [7] estimated $R_l = 5 \times 10^8$ cm, whereas N06 [9] estimated $R_l = 5 \times 10^{10} - 5 \times 10^{11}$ cm. These two estimates differ by 2–3 orders of magnitude! For the lower estimate, the wind cannot be thermally driven, whereas for the higher estimate it can. We note that the two groups also found different values for $R_{\rm IC}$ (i.e., M06's [7] estimate is 7×10^{12} cm whereas N06's [9] estimate is 5×10^{11} cm). Additionally, the two groups disagree about the gross properties of the thermal wind. In particular, contrary to N06 [9] , M06 [7] claimed that both theory and simulations (Begelman et al. 1983; Woods et al. 1996) [2] [1] predict mass-loss rates of thermal winds that are much too low to account for the observed density and blueshift.

The reason for the above disagreement can be traced down to the differences about the absorption lines of Fe XXII and Fe XXIII. N06 [9] assumed saturated lines and the absolute covering factor of the X-ray source to be 0.75, whereas M06 [7] took the lines to be unsaturated and used a covering factor of 1.

Miller et al. (2008) [10] confirmed their previous results and stated that if NO6's claim of the Fe XXII line being saturated were correct then the ratios of some other lines should be different than what is observed. Miller et al. also re-iterated their point that that Fe XXII lines are optically thin and that the covering factor along the line of the sight is near unity. They also stated that N06 [9] used too low a density (by factor of 5–10) as a consequence of his line saturation assumption.

The conclusion of M06 [7] and Miller et al. (2008) [10] was confirmed by Kallman et al. (2009) [39] who used spectral fitting to show that the ionization conditions in a 1-D model are not consistent with the wind being driven by thermal expansion.

Generally, M06 [7] , N06 [9] , and Kallman et al. (2009) [39] agree that thermal driving operates in this system but disagree about the properties of the thermal wind. Overall, it appears that thermal driving is unfavorable. However, this conclusion is based on simplified 1-D wind models and needs to be confirmed by a detailed physical model that takes into account the intrinsic multi-dimensional geometry of disk winds.

In this paper, we present 2.5-D axisymmetric, time-dependent hydrodynamical numerical simulations of thermally driven disk winds. We focus on the results obtained after the simulations reached the steady state and compare the results with observations. Our simulations do not include any magnetic processes and therefore do not address the possibility of the wind being magnetically driven, but they instead focus on the thermal contribution to the wind. The main goal of our simulations is to assess within the assumptions whether or not the thermally driven wind can account for the observations. We also consider possible implications of the fact that the mass-loss rate of the wind is several times higher than the total mass-accretion rate.

The paper is organized in the following way: Section 2 describes the methods used; Section 3 lays out the initial conditions of the simulation and discusses the properties of the fiducial run as well as its differences from other runs; Section 4 compares the results to the observations; Section 5 summarizes and discusses our results.

Method

Hydrodynamics

To compute the structure and evolution of a disk irradiated by the central source, we numerically solve the equations of hydrodynamics

$$\frac{D\rho}{Dt} + \rho\nabla \cdot \mathbf{v} = 0, \tag{2.8}$$

$$\rho \frac{D\mathbf{v}}{Dt} = -\nabla P + \rho \mathbf{g} \tag{2.9}$$

$$\rho \frac{D}{Dt}\left(\frac{e}{\rho}\right) = -P\nabla \cdot \mathbf{v} + \rho \mathcal{L}, \tag{2.10}$$

where ρ is the mass density, P is the gas pressure, $\mathbf{v}$ is the velocity, e is the internal energy density, $\mathcal{L}$ is the net cooling rate, and $\mathbf{g}$ is the gravitational acceleration of the central object. We adopt an adiabatic equation of state, $P = (\gamma - 1)\, e$, and consider models with the adiabatic index, $\gamma = 5/3$.

We use the ZEUS-2D code (Stone & Norman 1992) [6] extended by Proga et al. (2000) [5] to solve eqs. 2–4. We perform our calculations in spherical polar coordinates (r, θ, ϕ) assuming axial symmetry about the rotational axis of the accretion disk ($\theta = 0^o$).

Our computational domain is defined to occupy the angular range $0^o \leq \theta \leq 90^o$ and the radial range $r_{\rm i} \leq r \leq r_{\rm o}$. The numerical resolution consists of 200 cells in the r direction and 100 cells in the θ direction. In the angular direction, we used the following ratios: $d\theta_{\rm k+1}/d\theta_{\rm k}$=0.95, 0.97, 0.99, and 1.00 [i.e., the zone spacing increases towards the pole]. Gridding in this manner ensures good spatial resolution close to disk. In the r direction, we used $dr_{\rm k+1}/dr_{\rm k} = 1.04$, which enables a good resolution at smaller radii.

We chose the boundary condition at the pole (i.e., $\theta = 0^\circ$) as an axis-of-symmetry boundary condition. At the disk (i.e., $\theta = 90^\circ$), we applied the reflecting boundary condition. For the inner and outer radial boundaries, we used an outflow boundary condition (i.e., to extrapolate the flow beyond the boundary, we set values of variables in the ghost zones equal to the values in the corresponding active zones, see Stone & Norman 1992 [6] for more details).

Radiation Field

We deal with the radiation field and radiation heating and cooling in the the same manner as described by Proga et al. (2002; see also Proga et al. 2000) [4] [5] .

The net cooling rate is a function of the photoionization parameter, which is defined as:

$$\xi = \frac{4\pi \mathcal{F}_{\rm X}}{n}, \tag{2.11}$$

where $\mathcal{F}_{\rm X}$ is the local X-ray flux, $n = \rho/(m_{\rm p}\mu)$ is the number density of the gas. We consider fully ionized gas with $\mu = 0.6$. The local X-ray flux is corrected for the optical depth effects:

$$\mathcal{F}_{\rm X} = \mathcal{F}_{*} \exp(-\tau_{\rm X}), \tag{2.12}$$

where $\tau_{\rm X}$ is the X-ray optical depth and $\mathcal{F}_{*}$ is:

$$\mathcal{F}_{*} = \frac{\rm L_{*}}{4\pi r^2} \tag{2.13}$$

with $\rm L_{*}$ being the luminosity of the central source.

We estimate $\tau_{\rm X}$ between the central source and a point in a flow from

$$\tau_{\rm X} = \int_0^r \kappa_{\rm X} \rho(r,\theta)\ dr, \tag{2.14}$$

where $\kappa_{\rm X}$ is the absorption coefficient, and r is the distance from the central source. We assume $\kappa_{\rm X} = 0.4\,{\rm g}^{-1}\,{\rm cm}^2$ which is numerically of value of electron scattering. We found that in most cases, the wind is optically thin and the wind column density,

$$N_H(\theta) = \int_{r_i}^{r_o} \frac{\rho(r,\theta)}{\mu m_{\rm p}} dr \tag{2.15}$$

is less than $10^{23}\,{\rm cm}^{-2}$.

Results

To complete the specification of the simulations, we need to assign the properties of the disk atmosphere (the lower boundary condition for the wind solution). For the density, we use a simple distribution at $\theta = 90^\circ$ of the form: $\rho = \rho_o (r/r_{\rm IC})^{-\alpha}$, where α and ρ_o are constants. We run the model for $\alpha = 0$, 1, 2, and 3 and for $\rho_o = 10^{-12}$, 10^{-11}, and 10^{-10} g cm^{-3} (see table 1). The temperature is set to 10^4 K, while the radial velocity is set to zero. In addition, we enforce Keplerian rotation at $\theta = 90^\circ$. The size of the computational domain is defined in the following way: $r_{\rm i} = 0.05\, R_{\rm IC}$ while $r_{\rm o} = 20\, R_{\rm IC}$. We follow M06 [7] and N06 [9] and adopt the following properties of the system: the mass of the central black hole $\mathrm{M_{BH}} = 7\ \mathrm{M_\odot}$, the luminosity $\mathrm{L_*} = 0.03$ in units of the Eddington limit, $\mathrm{L_{Edd}}$, and the Compton temperature, $T_{\rm IC} = 1.4 \times 10^7$ K. The adopted L_* corresponds to the mass accretion rate $\dot{M}_{\rm a} = 4.4 \times 10^{17}$ g s^{-1}.

Properties of the Fiducial Run

Our fiducial run (C8) has the following parameters: α=2, $\rho_o = 10^{-11}\, g\, \mathrm{cm}^{-3}$, $d\theta_{\rm k+1}/d\theta_{\rm k} = 0.97$, $dr_{\rm k+1}/dr_{\rm k} = 1.04$. This run settles to a steady state after about 3 sound-crossing times.

We show the geometry and structure of the fiducial run in figure 2. The top left panel shows a density distribution with a significant departure from spherical symmetry.

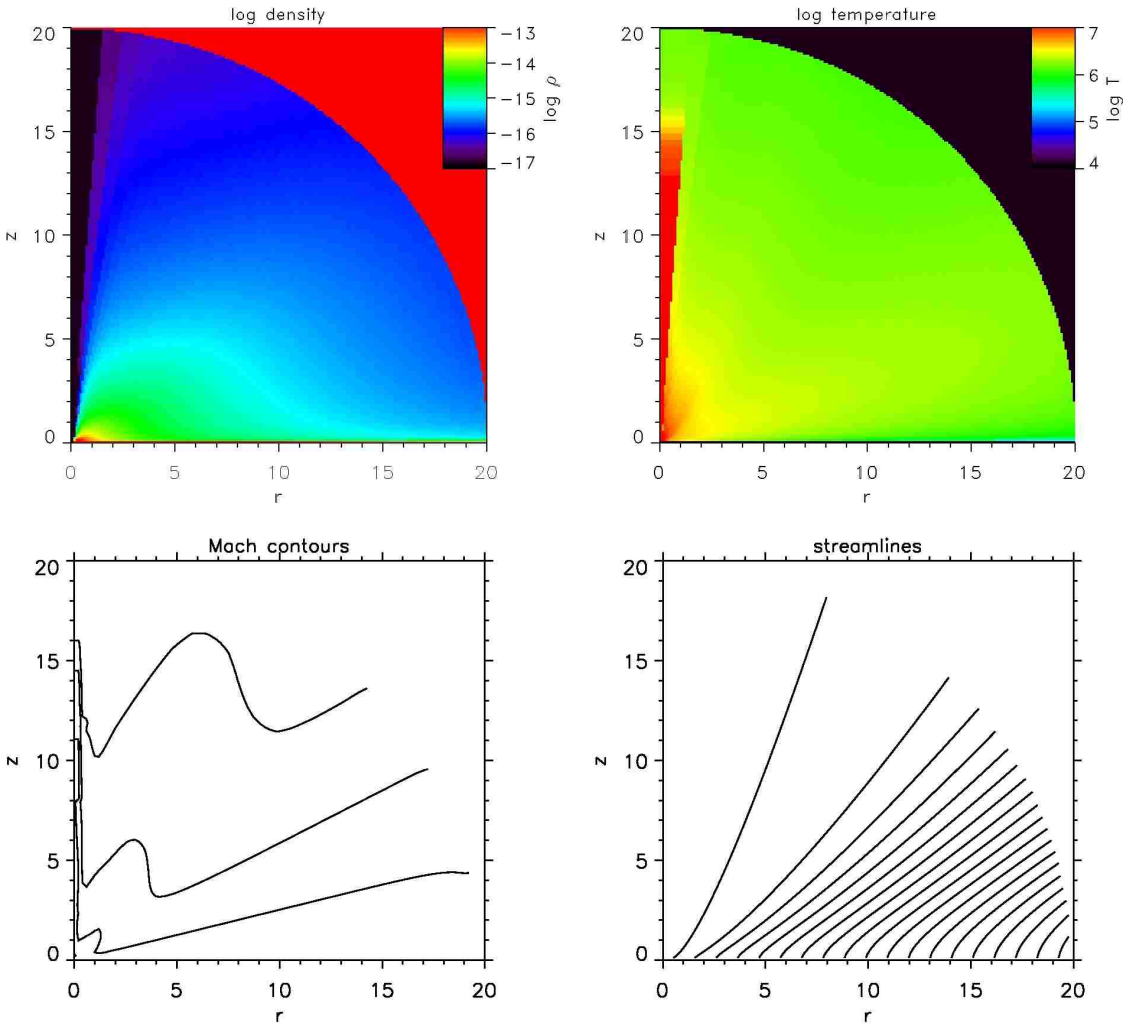

Figure 2 The fiducial run C8. *Top left panel:* Color density map. *Top right panel:* Color temperature map. *Bottom left panel:* The Mach number M contours (the poloidal component only). Contours are for M = 1, 2, and 3 (bottom to top). *Bottom right panel:* The flow streamlines. Note the self-similarity of the streamlines especially those arising from the outer disk. In all panels the rotation axis of the disk is along the left-hand vertical frame, while the midplane of the disk is along the lower horizontal frame. Lengths are expressed in units of the Compton radius, $R_{\rm IC}$.

The temperature (top right panel) is close to 0.1 $T_{\rm IC}$ in the outer part of the wind. In a very narrow region around the rotational axis, the temperature is much less than $T_{\rm IC}$ at $r > 16R_{\rm IC}$, whereas at the small radii the temperature is comparable to $T_{\rm IC}$. The X-ray irradiated gas accelerates rapidly and becomes supersonic relatively close to the disk. As shown in the bottom left panel, the contour for the Mach number of one corresponding to the wind launched at relatively large radii is almost a straight line making an angle of about 15° with the disk midplane. Streamlines (bottom right panel) show that most of the disk wind follows almost perfect straight lines inclined at the angle of about 45° with respect to the disk midplane. The streamlines are curved only in zones near the rotational axis and very close to the disk. It appears that the outer wind is self-similar (we will return to this point at the end of this subsection). The streamlines also show that the flow expands in the angular direction, reminiscent of a spherical outflow, only for streamlines originating at $r \lesssim 3\ R_{\rm IC}$.

An accretion disk is geometrically extended and as such it intercepts the central radiation over a large range of radii. However, the thermal expansion drives a significant wind only within a relatively narrow radial range. One can show this wind property by plotting the product of the density and the velocity normal to the disk as a function of the radius along the disk midplane (see figure 3).

Most of the outflow in the fiducial run comes from the narrow ring on the disk in the zone between $0.07\,R_{\rm IC}$ and $0.2\,R_{\rm IC}$ having its maximum at $\sim 0.1\,R_{\rm IC}$. For radii $> 0.2\,R_{\rm IC}$ the mass flux density scales like r^{-q}, with $q = 1.76$.

The wind is launched in a non-spherical way and it remains non-spherical as it expands. To illustrate this point, figure 4 shows various flow properties at $r_{\rm o}$ as functions of θ. In particular, the top panel shows the product of density and radial velocity (solid line) and the accumulated mass-loss rate (dotted line).

We evaluate the accumulative mass-loss rate throughout $r_{\rm o}$ using the following

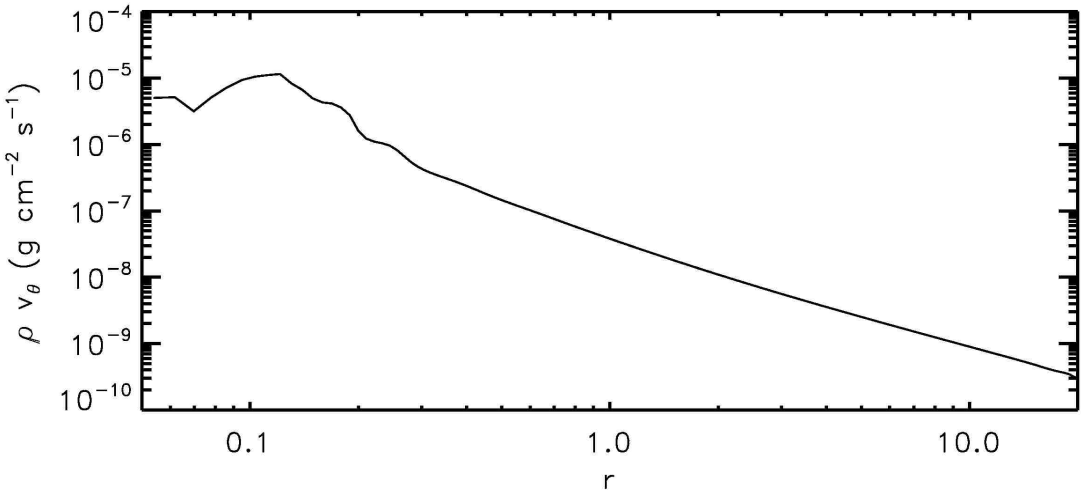

Figure 3 The mass flux density, ρv_θ, as the function of radius along the disk midplane, $\theta = 90^\circ$ for the fiducial run.

formula:

$$d\dot{m}(\theta) = 4\pi {r_\mathrm{o}}^2 \int_{0^\circ}^{\theta} \rho v_\mathrm{r} \sin\theta d\theta. \tag{2.16}$$

One finds that most of the mass flows out of the computational domain through the outer spherical boundary over a broad range of angles between 20° and 75°. The outflow for large θ contributes insignificantly. The total mass-loss rate for the fiducial run is $\dot{M}_\mathrm{w} = d\dot{m}(90^\circ) = 3.3 \times 10^{18}\,\mathrm{g\,s^{-1}}$. Note that this is larger than the assumed accretion rate $\dot{M}_\mathrm{a}$ by a factor of 7.5. We will return to this point in Section 5.

The middle panel of figure 4 shows that the photoionization parameter (solid line) decreases with increasing θ, which is another indication that the wind is not spherically symmetric. In particular, ξ changes from 10^5 to 10^3, whereas the column density (dotted line) increases from below $10^{21}\,\mathrm{cm^{-3}}$ to $10^{23}\,\mathrm{cm^{-3}}$.

The bottom panel of figure 4 presents the radial velocity (solid line) and the number density (dotted line) vs. θ. It is evident from this panel why the zones close to the disk and the rotational axis contribute insignificantly to the total mass-loss

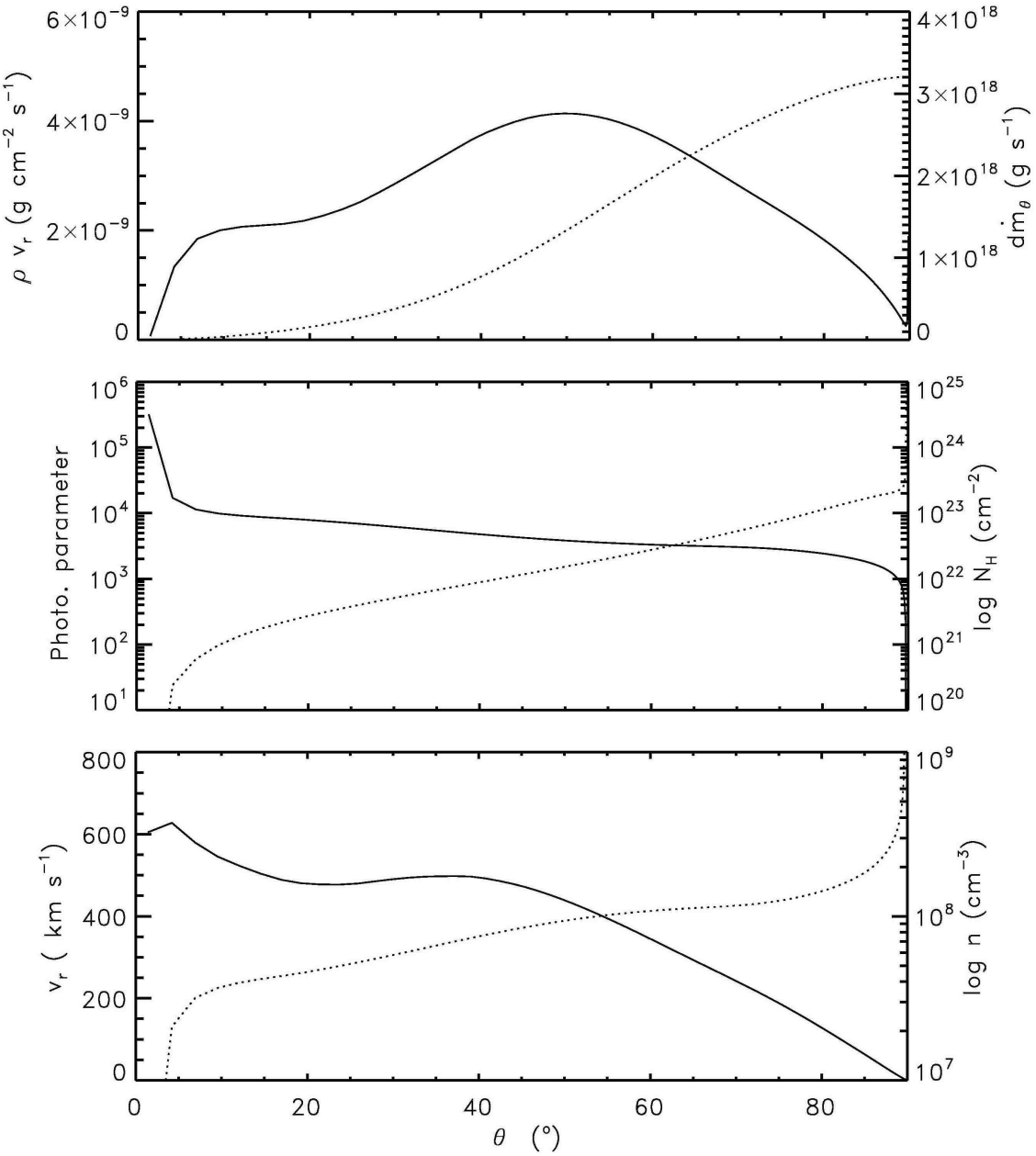

Figure 4 Quantities at the outer boundary, $r_{\rm o}$ of the fiducial model. The ordinate on the left hand side refers to the solid line, while the ordinate on the right hand side refers to the dotted line. *Top panel:* Mass flux density and the accumulative mass-loss rate. *Middle panel:* Photoionization parameter and the column density. *Bottom panel:* radial velocity and number density.

rate: the zone near the disk is very dense but also very slow, while the zone near the axis of rotation has extremely low density, so that the product of the density and radial velocity is very small.

To specify the departure of the disk wind from a purely radial wind, figure 5 shows ξ (top panel) and n (bottom panel) as a function of radius for various θ.

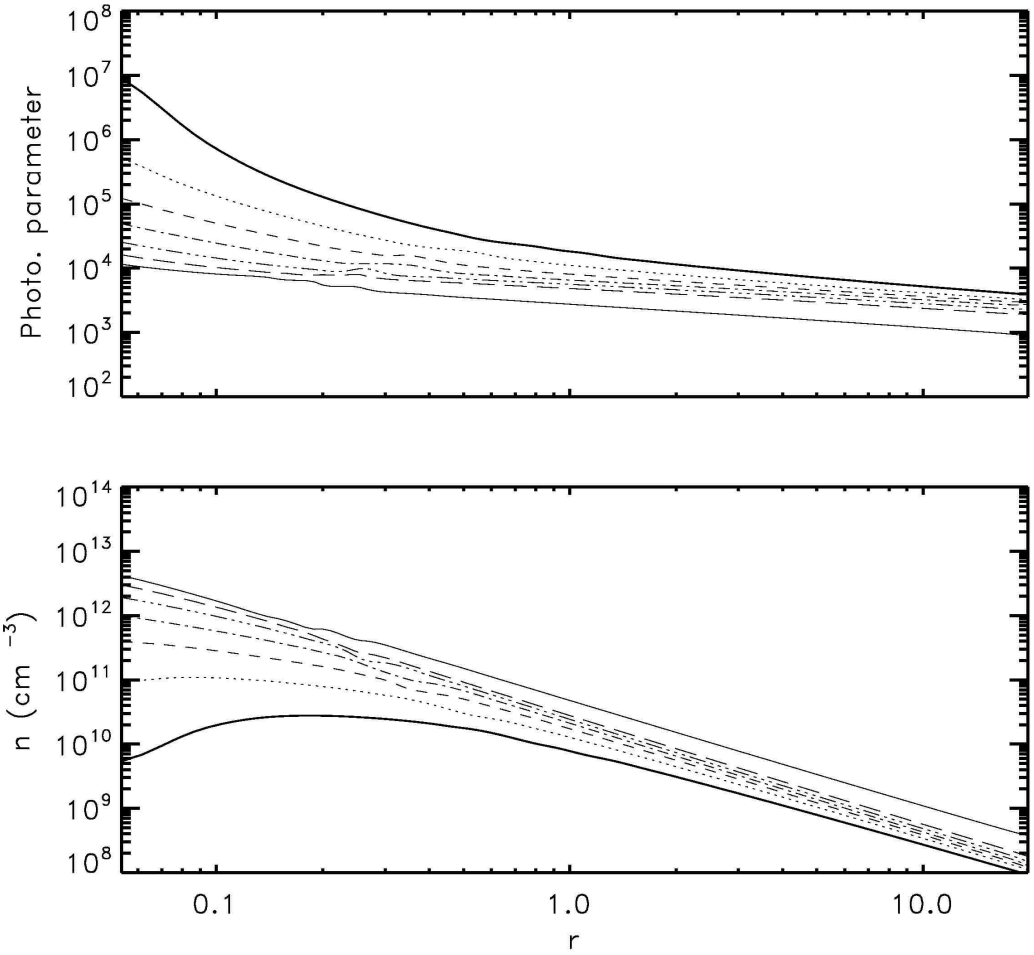

Figure 5 The radial profiles of the photoionization parameter (top panel) and the number density (bottom panel) for seven polar angles along the radius for the fiducial run. The angles are: $\theta = 48.3°$ (thick solid), $\theta = 60.5°$ (dotted), $\theta = 69.4°$ (dashed), $\theta = 76.0°$ (dot-dashed), $\theta = 80.9°$ (triple dot-dashed), $\theta = 84.5°$ (long dashed) and $\theta = 89.1°$ (thin solid). Note that a simple spherically expanding outflow poorly approximates the disk wind solution (see the main text for more details).

In the case of an optically thin radial wind with a constant velocity, ξ is constant and $n \propto r^{-2}$. In our solution, ξ decreases with increasing radius especially for small and intermediate θ, whereas n decreases slower than r^{-2} and can even increase with radius for $\theta < 62°$.

How does our solution compare to a β-velocity law, in terms of approaching a constant value at large r? As expected, it is in agreement for large radii. Figure 6 shows an example of the radial velocity as a function of radius for $\theta = 76^o$ (this corresponds to the dot-dashed lines in Fig. 4).

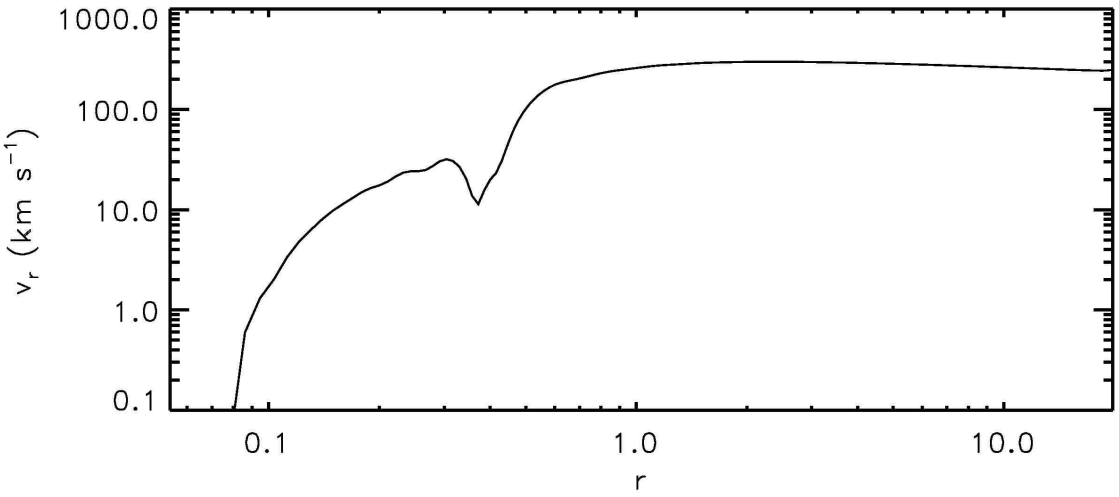

Figure 6 Radial velocity as the function of radius at $\theta = 76°$ for the fiducial run. The non-monotonic radial profile demonstrates that the disk wind is not radial (see also Fig. 4).

The radial velocity increases up to the Compton radius and then remains roughly constant. Also, there is a visible dip at 0.4 R_{IC}, which is a consequence of the radial line crossing different streamlines. The function has a nearly flat shape for radii larger than $1.0\,R_{IC}$.

We conclude that a thermal disk wind can not be approximated by a radial outflow. Font et al. (2004) [29] found that a disk wind expands quasi-spherically if a

relatively steep decline of the mass flux density with radius is assumed ($\rho v_\theta \propto r^{-q}$, with $q \gtrsim 2.5$). As we mentioned above, in our self-consistent simulations, $q \approx 1.76$ in the self-similar part of the wind. It is unfortunate that the wind expansion is non-radial because a radial outflow is a very simple case that can be (and has been) straightforwardly implemented into photoionization/spectra calculations. Is it then possible to approximate the thermal wind with some other simple model? It is beyond the scope of this paper to answer this question.

Comparison of the Fiducial Run With Other Runs

To check the robustness of the solution presented above, we explored effects of the numerical resolution and the density along the lower boundary. We present the most significant properties of those runs in Table 1 . The columns are organized in the following way: (1) the name of the run; (2) the α parameter used in the density profile; (3) $\rho_{\rm o}$, the normalized density at the lower boundary of the computational domain; (4) $d\theta_{\rm i+1}/d\theta_{\rm i}$, the angular resolution; (5) $\rho(r_{\rm in})$ the disk density at the inner radius; (6) $\dot{M}_{\rm w}$ the total wind mass-loss rate; (7) the maximal angle $\theta_{\rm max}$ for which the integration of the total wind mass-loss is computed [$\dot{M}_{\rm w} = d\dot{m}(\theta_{\rm max})$]; (8) the maximal radial velocity on the outer shell; (9) the total time of the run.

As mentioned in the Section 3, the density along the lower boundary ($\theta = 90^\circ$), is specified by two parameters, α and $\rho_{\rm o}$. We have run several models for various α and $\rho_{\rm o}$ to check if our solution depends on the density along the disk. As for radiation driven disk winds (see e.g., Proga et al. 1998) [40] , we find that as long as the density along the disk is high enough, the gross properties of the thermal disk wind do not depend on the assumed disk density.

For a relatively small density along the disk, the X-rays heat the gas to the Compton temperature even at $\theta = 90^\circ$. This means that the computational domain does not capture a cold disk and its part that is in hydrostatic equilibrium. Consequently,

Table 1 Summary of the disk wind results

No. of run	α	ρ_o ($\mathrm{g\,cm^{-3}}$)	$d\theta_{i+1}/d\theta_i$	$\rho\,(r_{in})$ ($\mathrm{g\,cm^{-3}}$)	$\dot{\mathrm{M}}_{\mathrm{wind}}$ ($10^{18}\,\mathrm{g\,s^{-1}}$)	θ_{max} (°)	v_r ($\mathrm{km\,s^{-1}}$)	t_f (2.2×10^5 s *)
A	0	10^{-10}	0.97	10^{-9}	0.33	59	587	10
B	1	10^{-10}	0.97	10^{-9}	0.33	67	599	10
C1	2	10^{-12}	1.00	10^{-10}	6.6	90	746	10
C2	2	10^{-12}	0.99	10^{-10}	6.8	90	708	10
C3	2	10^{-12}	0.98	10^{-10}	6.9	90	675	10
C4	2	10^{-12}	0.97	10^{-10}	7.0	90	642	10
C5	2	10^{-12}	0.96	10^{-10}	7.1	90	619	10
C6	2	10^{-12}	0.95	10^{-10}	7.1	90	604	30
C7	2	10^{-11}	0.99	10^{-9}	0.32	90	703	10
C8	2	10^{-11}	0.97	10^{-9}	0.33	90	627	10
C9	2	10^{-11}	0.95	10^{-9}	0.33	90	587	10
C10	2	10^{-10}	0.99	10^{-8}	0.33	63	692	30
C11	2	10^{-10}	0.97	10^{-8}	0.33	62	603	30
C12	2	10^{-10}	0.95	10^{-8}	0.33	63	553	10
D1	3	10^{-11}	0.97	10^{-8}	0.11	90	670	10
D2	3	10^{-10}	0.97	10^{-7}	0.32	90	621	30

* 2.2×10^5 s is the sound crossing time = (r_o/c_s), calculated for T=T_{IC}.

the simulations do not follow the transition between a cold and a hot flow. Therefore, the mass flux density from the lower boundary is set not by the physics of a cold disk being heated by X-rays but by a choice of the density. Comparing $\dot{M}_{\mathrm{w}}$ for runs C4, C8, C11, and D2, we find that the mass-loss rate depends on the density if the density is too low. Only when the density along the disk is high enough that the central X-rays do not heat the gas along the lower boundary, the simulations capture the transition from the cold to hot phase. The mass-loss rate then becomes independent of a particular choice of the density in the cold part of the disk.

However, we also find that for very high densities along the disk there is a technical problem with a proper measurement of $\dot{M}_{\mathrm{w}}$. Our goal is to compute a wind from a geometrically thin disk. But if we choose too a high density along the lower boundary, the disk will flare and its thickness at large radii becomes substantial. During the simulations, the dense disk remains cold and nearly in hydrostatic equilibrium but it will subsonically fluctuate. Therefore, when computing the *wind* mass-loss rate,

one needs to keep in mind these fluctuations of the dense disk and exclude the region very close to the disk midplane. Otherwise the subsonic oscillations of the very dense disk material would be counted as the disk outflow and this will yield an erroneous estimate of the wind mass loss rate. In practice, when calculating the total outflow rate for some runs, we stop the integration in eq. 10 at $\theta_{\rm max} < 90^o$, where the transition from the wind to the disk occurs. This transition is not difficult to identify as it occurs where the density sharply increases with θ (see the bottom panel in Fig. 3). The seventh column in Table 1 lists the maximum angles we used.

For the fiducial run as well as some other runs, the region near the disk midplane does not affect estimations of $\dot{M}_{\rm w}$. This is one of the reasons we chose the run C8 with $\rho_{\rm o} = 10^{-11}\,{\rm g\,cm^{-3}}$ as the most suitable run in terms of having not too high a density, as only a small portion of the dense disk will enter the domain. On the other hand, the density cannot be so small as to make the transition from the disk to the wind outside the computational domain. All runs with the density comparable to or larger than that in the fiducial run have a total mass-loss rate of about $3.3 \times 10^{17}\,{\rm g\,s^{-1}}$. Other wind properties are also similar (see Table 1).

As for the resolution study, we find that changes in the $d\theta_{\rm k+1}/d\theta_{\rm k}$ factor produced small differences of the final steady state and such effects just slightly changed calculated physical quantities and properties of the solution.

Comparison with Observations

We start our comparison with the observations by considering the wind properties inferred from the observation and then we present an example of the synthetic spectrum directly compared with the observed X-ray spectrum. As we described in Section 1, the number density of the wind is inferred to be quite high, i.e., 5×10^{15} cm^{-3}.

Figure 7 shows the scatter plot of the photoionization parameter vs. $v_{\rm r}$ based on run C8.

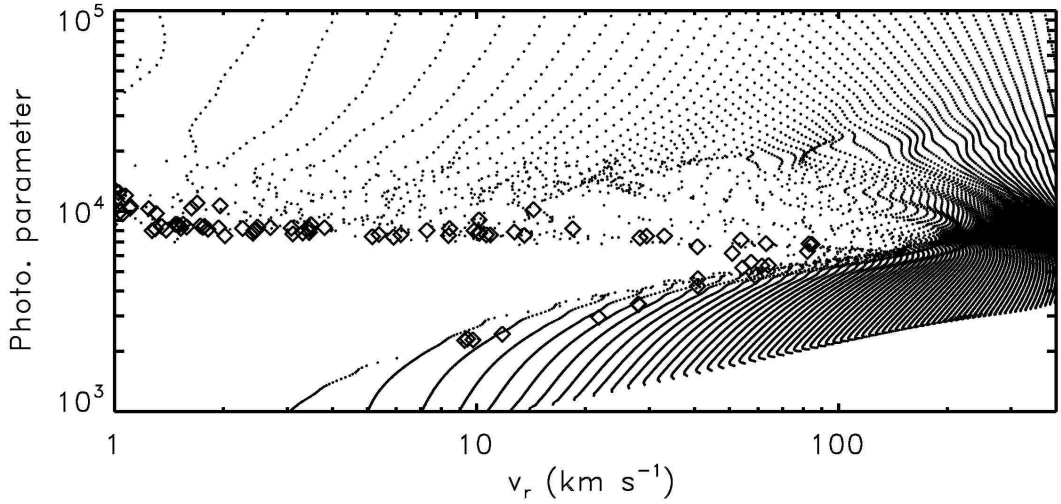

Figure 7 Scatter plot of photoionization parameter vs. v_r for the fiducial run. Dots correspond to $n < 10^{12}$ cm^{-3} whereas diamonds correspond $n \geq 10^{12}$ cm^{-3}. The lack of points corresponding to $v_r > 100$ km s^{-}1 means that the thermal wind can not account for a high density fast outflow as observed in GRO J1655–40 during an X-ray-bright state.

Dots correspond to $n < 10^{12}$ cm^{-3}, whereas diamonds correspond $n \geq 10^{12}$ cm^{-3}. Note that there are *no diamonds* corresponding to $v_{\rm r} \geq 100\,{\rm km\,s^{-1}}$. This means that our model fails to predict the wind density and velocity as inferred from the observations. We stress that in the computational domain of our simulation there is gas with densities as high as $n \approx 5 \times 10^{15}$ cm^{-3}, but this high density gas is very slow (e.g., the bottom panel of Fig. 3). This simple comparison shows that our results support M06 [7] and Kallman et al.'s (2009) [39] conclusion: a thermal wind can not account for the X-ray observations.

As another test of our model, we computed synthetic spectra using the photoionization code XSTAR (Kallman & Bautista 2001; Bautista & Kallman 2001). [41] [42] Our method of making this calculation is very similar to that used and described in Dorodnitsyn et al. (2008) [43] . We have computed spectra of the fiducial model for several inclination angles. We have also calculated the emissivity and opacity at each

point in the hydrodynamic flow at the end of the simulations, and then integrated the formal solution of the transfer equation along radial rays to get the spectrum. In doing this we ignore emission. Since emission will tend to fill in absorption lines, thus reducing their strength, these models represent an overestimate to the amount of absorption coming from such a flow. For most inclinations, the spectra show no absorption features or only very weak ones. Figure 8 compares the count spectrum observed by the HETG during an X-ray bright phase of the GRO J1655–40 2005 outburst (see M06 [7] for more details) with an example of our synthetic spectrum.

For this figure (8), we have chosen an almost 90° inclination because it yields the best fit to the data and the right ionization for the most lines. Nonetheless, even for this very high inclination, the range of ionization is too narrow, and the ionization is probably lower than that observed. It is possible to obtain higher ionization for lower inclinations, but then the column density is lower, making the fit is even worse. To see if we can improve the fit for a given density structure, we have to put in the 600 km s^{-1} blueshift by hand while computing this spectrum (note that our wind model does not predict such a high velocity of the dense wind at this inclination angle). However, neither this nor any other simple model fits the Fe Kα line profile showing the high velocity ($\sim$1600 km s^{-1}) component. We found also that the curve-of-growth of the lines does not fit: there are no saturated lines in the model. Still, close to half of the observed lines are predicted in the model, including the Fe XXII lines.

In addition to an inadequate mass loss rate, the model shows a geometric structure different from that required by spectra of GRO J1655–40. From the lack of emission lines, M06 [7] and N06 [9] concluded that the global covering factor of the wind is small, while figure 4 shows that the density is reasonably constant over a broad range of angles.

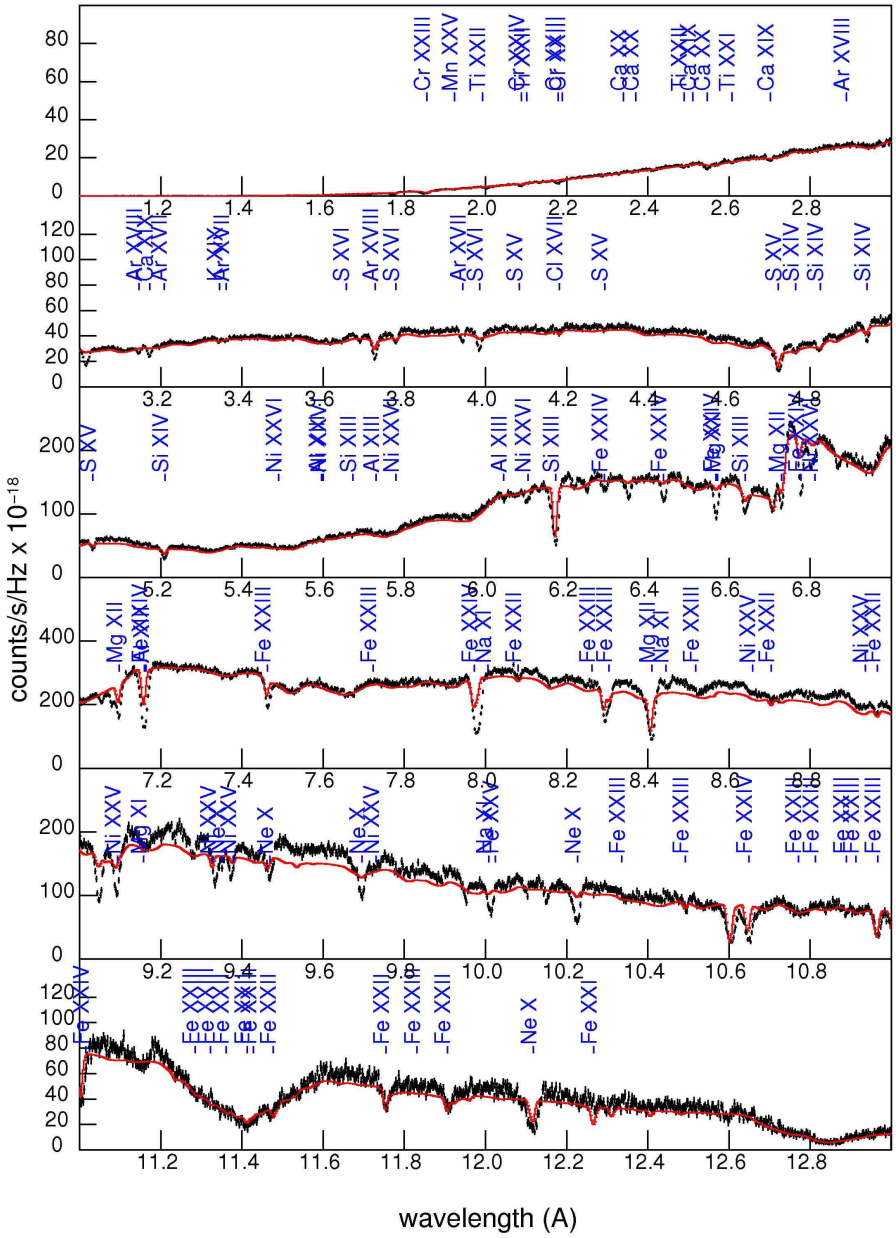

Figure 8 Comparison of the X-ray spectrum of GRO J1655–40 with the model spectrum computed based on our thermal disk wind (see Section 4). The points with the error bars are the data and the model is the red curve. The wavelength in Angstroms.

Summary and the Discussion

In this paper, we presented axisymmetric, time-dependent hydrodynamical numerical simulations of thermally driven disk winds. To apply our results to GRO J1655–40, we adopted the observed mass of its black hole, and the properties of its X-ray radiation. We performed the simulations using the same code and in a similar fashion to PK02 [4] who computed wind for low-mass X-ray binaries. The main difference is that we turned off the radiation driving here because as found by PK02 [4] it is negligible for the stellar black hole accretors. Turning off the radiation driving makes the simulations run much faster. The main goal of our simulations is to check whether, in the absence of magnetic fields and within the given simplifications and assumptions, the thermally driven wind can account for the observation.

To compare the results with the observations, we also computed transmitted X-ray spectra using the photoionization code XSTAR and our wind solution. Our main findings are:

1) The density of the fast-moving part of the wind is more than one order of magnitude lower than that inferred from the observations. Consequently, contrary to the claim made by N06 [9] , the thermal model fails to predict synthetic spectra with line absorption as strong and as blueshifted as those observed. Overall our results support the conclusion reached by Miller et al. (2008) [10] and Kallman et al. (2009) [39] , that GRO J1655–40, and likely other X-ray transient sources, have thermal winds insufficient to explain the observed spectra;

2) Despite the thermal wind being weak and Compton thin, the ratio between the mass-loss rate and the mass accretion rate is about seven;

3) We discovered that the outer wind is self-similar.

One should ask if our simulations are conclusive. Namely, can we rule out thermal driving as a mechanism responsible for the observed wind even though we did not

consider some effects such as thermal conduction? Conduction could increase the degree of disk heating and could in principle increase the gas density above the disk photosphere. However, it is unclear if this increase would lead to an increase in the density at the wind base and consequently in an increase of the density of the fast wind, which is what is needed to account for the observations. The density of the wind base also could be sensitive to the details of radiative transfer and spatial resolution. Hydrostatic models of the ionization layer on the surface of the disk by Jimenez-Garate et al. (2002, 2005) [44] [45] showed that there is much more opacity than the electron scattering opacity in the very thin layer that produces UV and most of the X-ray emission on top of the optically thick disk. Therefore, our pure electron scattering assumption might underestimate the opacity. However, if this were true then that would mean that thermal driving is even less efficient because the irradiation would penetrate the disk even less. We expect that the mass loss rate is set at the sonic point, which would occur in the million Kelvin temperature plateau seen in the hydrostatic models. In that region, the models indicate that photoabsorption opacity due to Fe XXV and Fe XXVI is comparable to the electron scattering opacity. The radiative heating also can be affected by disk flaring or the shape of the disk, in general. For example, at a given radius a strongly flared disk might intercept more central radiation than a flat disk. Consequently, a resulting outflow might be more collimated and denser. We intend to extend our model to explore these effects in near future. However, before that we plan to check if the inclusion of magnetic driving will produce a dense fast wind.

It is important to remember that the outburst spectra of GRO J1655–40 and GRS 1915+05 are exceptional. Spectra of these objects in their low states, as well as spectra of other black hole binaries, show absorption lines of only Fe XXV and Fe XXVI. That suggests lower densities and mass loss rates, and it raises the question of whether thermally driven winds might account for those observations. The micro-

quasar H1743−322 (Miller et al. 2006) [46] is a good example, with Fe XXV and Fe XXVI equivalent widths of up to 4.3 mÅ and 6.8 mÅ, respectively. The densities are below 10^{13} cm^{-3} and the ionization parameters are above 10^5 in 4 separate observations. We have examined our models at sightlines farther from the disk, where the velocities match those reported by Miller et al. (2006) [46]. The Fe XXV and Fe XXVI column densities are too small to account for the observed equivalent widths by a factor of a few, and we conclude that thermally driven winds cannot account for the typical low state winds.

In the models presented here, we found that $\dot{M}_{\rm w}/\dot{M}_{\rm a} \approx 7$. This is a fairly large ratio, which could mean that the thermally driven wind can significantly change the mass flow in the disk. Therefore, we decided to check if our result is consistent with the results of others who modeled thermally driven winds. Of particular interest is work by Woods et al. (1996) [1] , who studied thermally driven disk winds in great detail and performed many axisymmetric wind simulations for various luminosities. They summarized their results in an analytic formula which fitted the mass flux density distribution obtained from simulations for various L_* (their eq. 5.2).

To find $\dot{M}_{\rm w}\,/\,\dot{M}_{\rm a}$ predicted by Woods et al.'s simulations, we integrated their formula over the disk surface to obtain $\dot{M}_{\rm wind}$ and then expressed L_* through the following equation of the accretion luminosity:

$$L_* = \frac{\rm G\,M_{BH}\,\dot{M}_a}{2\,r_s}, \tag{2.17}$$

where $r_{\rm S}$ is the Schwarzschild radius, which yields a relation between $\dot{M}_w$ and $\dot{M}_a$. We found that Woods et al. simulations predict $\dot{M}_{\rm w}\,/\,\dot{M}_{\rm a}$ in a range from 2.0 to 6.0 depending on the luminosity. The L_* dependence is weak for $L_*/L_{\rm Edd} < 0.1$. Thus $\dot{M}_{\rm w}\,/\,\dot{M}_{\rm a}$ is higher than, but comparable, to Woods et al.'s results for L_* on the lower side of their luminosity range. Nevertheless, both set of simulations predict

$\dot{M}_{\rm w} \,/\, \dot{M}_{\rm a} > 1$.

Our conclusion from this analysis is that $\dot{M}_{\rm w}$ is greater than the rate at which the central engine is fueled. This in turn can make the disk variable. One could even expect this relatively strong wind to cause a recurrent disappearance of the inner disk even if the disk is fed at a constant rate at large radii. Neilsen & Lee (2009) [34] suggested such a process while interpreting jet/wind/radiation variability in the microquasar GRS 1915+105. It is beyond the scope of this work to model the effect of the wind on the disk. However, this problem was studied by Shields et al. (1986) [3] , who showed that due to viscous processes no oscillations appear for $\dot{M}_{\rm w} \,/\, \dot{M}_{\rm a} < 15$! We conclude that the thermal wind is to weak to cause the oscillation. But the thermal wind is also too weak to account for the observed wind. Therefore, it is possible that in GRO J1655–40, and other sources, e.g., GRS 1915+105, the wind responsible for the observed X absorption will be so strong that $\dot{M}_{\rm w} \,/\, \dot{M}_{\rm a} > 15$ and as such cause disk oscillations and contribute to the observed disk variability.

Follow–up Research on This Paper

We did the follow–up research on the self–similar properties of the streamlines. However, as we noted earlier, the outer part of the disk wind solution appears to be self–similar. Our detailed analysis of the geometry of the streamlines confirms their self–similarity. For example, the left panel of the figure 9 compares the streamlines from the fiducial run, rescaled and plotted on the scale from 0 – 100 $\rm R_{IC}$,with the streamlines from a rerun of the fiducial run, with $r_{\rm o} = 100$ instead of 20 $\rm R_{IC}$. Far from the inner and outer edge of the solution, the two sets of streamlines are very similar to each other. Thus, one shape of a streamline can fit various streamlines.

To determine this universal shape of the streamline, the right panel of figure 9 shows the streamlines from the fiducial run (on the 0 - 20 $\rm R_{IC}$ grid), after rescaling them according to the following formulae: $z'_i(j) = z_i(j)\,\frac{r_1(0)}{r_{\rm i}(0)}$; $r'_i(j) = r_{\rm i}(j)\,\frac{r_1(0)}{r_{\rm i}(0)}$, where

i is the order number of the streamline and j is the number of the point along a given streamline.

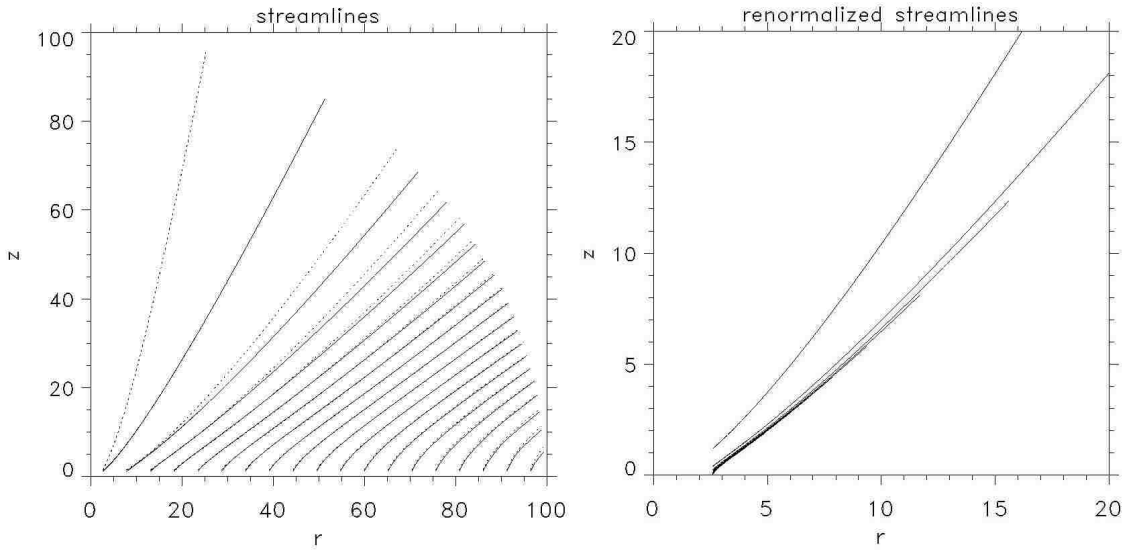

Figure 9 Self–similarity of the thermal disk wind. *Left panel:* Comparison between the streamlines for a rerun of the fiducial run on the grid with the outer radius 100 R_{IC} instead of 20 R_{IC} (dotted lines) and for the fiducial run (solid lines). The streamlines of the fiducial run are rescaled by a factor of 5 to fit in the 100 R_{IC} grid. A close overlap of the lines from the two simulations, that were run on two different scales, indicates the self–similar nature of the solution. *Right panel:* The streamlines of the fiducial run renormalized according to eq. 11. Note that, except for the two lines arising from the inner disk, all the other lines have very similar shapes and are almost indistinguishable.

This rescaling again reveals a striking similarity of the streamlines that originate far from the inner edge of the solution. As Fig. 1 shows, the shape of the streamline can be approximated as a vertical line near the disk surface that quickly bends outwards and becomes a straight line. One can then fit the streamlines into the zone of the self–similarity with a simple formula. Specifically, the streamline starting at 5.5 R_c can be very well fitted by the following formula:

$$z(r) = [1 - \exp(-6.4\,r)] \times (0.41 + 0.71\,r + 0.0089\,r^2). \qquad (2.18)$$

Note that the quadratic term is very small, compared to the linear term. The exponential part of the formula is used to capture the vertical part of the streamline, near the disk and its subsequent turn into a straight line away from the center and the disk.

This analysis is very encouraging, and we plan to derive the self–similar solution of the thermal disk wind by solving the hydrodynamical equation analytically, or semi–analytically. However, one needs to keep in mind that the majority of the mass–loss does not come from the self–similar region. Therefore, the usefulness of the self-similar solution might be limited.

We emphasize the significance of this proposed model with an accent on interpreting the data. We present the most commonly used models of disk wind geometry on the figure 10 . Observers interpret their data based on assumptions about the density distribution and the geometry of the flow. Our model does not predict simple power law for the density distribution, most commonly used as an assumption by the observers, which was discussed in detail in this chapter. Regarding the geometry of the flow, our model does not predict spherically symmetric and diverging cases, which are often used, and instead suggests a geometry with streamlines being parallel and at a given angle with respect to the disk as shown on the figure 10 . Hopefully, this model will be taken into account by observers and the consequences of changing their assumptions will be quantified and revealed.

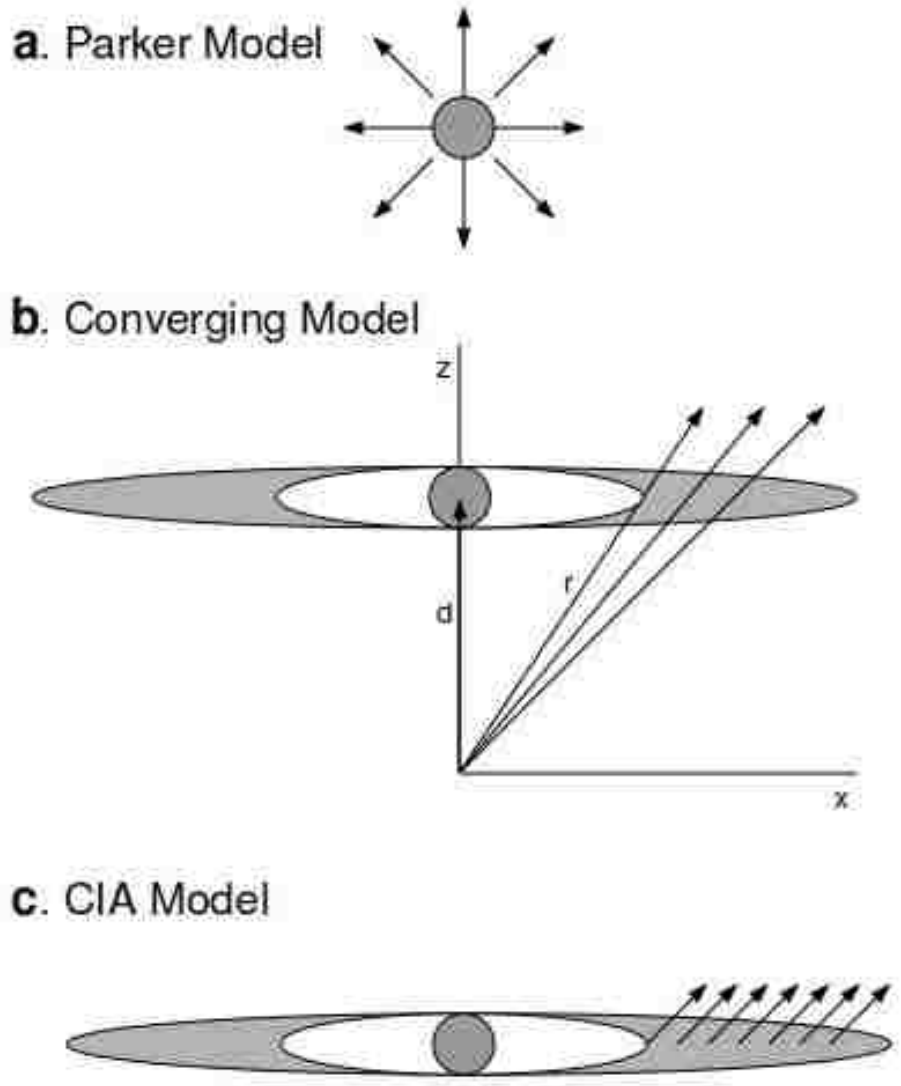

Figure 10 Three different models for disk winds, top panel: spherically simmetric case, middle panel: diveging case and the CIA case on the bottom panel. (Image by T. Waters)

Connection with the Extrasolar Planet Wind Problem

In the next chapter, we present the numerical simulations and the analysis of the results of the wind arising from the extrasolar planet interacting with the wind from the parent star. In this chapter, the accretion disk is simplified as a fully axis symmetric object. The heated surface is a disk. To analyze extrasolar planets, we are the using same method. However, in this case we are creating a spherically heated surface, with a defined distribution of temperature. In order to analyze spherical objects in circular orbit, we will use 3D software to include all nonsymmetric effects. In essence, this 3D problem is analyzed using this same approach as the previous 2.5D problem, only using different geometry and boundary conditions, and, of course, with a different physical background.

CHAPTER 3

EXTRASOLAR PLANETS WINDS

Brief Introduction to Athena 3D Code

The Athena 3D is the code developed by the same authors as Zeus 2D. It is written in C while Zeus is written in Fortran. They have many similarities, but Athena has more advanced numerical solvers incorporated into it, and it is much more suitable to implementing more physical equations driving the system than those originally anticipated by the authors. Being more flexible in this manner, it allows the user to write scripts which can easily be incorporated into the code. We were, on the one hand, motivated to use Zeus 2D because it is a very well–tested and acknowledged code, which deals well with accretion disk–type problems and similar geometries. On the other hand, our research group has plenty of experience with it [5] [4] , and has been applying it to a wide range of astrophysical problems in the past. When considering extrasolar planet problems, it would be possible to conclude that they may be investigated using two dimensional software, but due to the motion of the planet on the circular orbit, the planets' system is subject to Coriolis force and moves through the medium. In order to acquire a deeper grasp of the problem, the necessity for a three dimensional simulation arose. We, therefore, swithched to Athena 3D. Athena uses completely different algorithms, mainly focusing on Godunov methods [47] and and Reimann solvers [48] . The possibility of a logarithmic scaling of the grid (which gives the user a decent edge by saving on computational time when there are zones of the computational domain and where a much higher resolution is required due to the physical setup) is lacking in Athena. This is one of its major drawbacks. Yet overall Athena seems to be the best possible choice today compared to the other codes available for the types of problems we are dealing with.

Athena 3D is a numerical code for magnetohydrodynamics. It uses a single step,

second–order accurate, Godunov scheme for ideal MHD, which is an extension of the method described in (T.A. Gardiner, J.M. Stone, 2005, 2007) [49] [50] . This algorithm combines the corner transport upwind method of Colella [51] for multidimensional integration, and the constrained transport algorithm for preserving the divergence–free constraint on the magnetic field. It compares two different forms for the corner transport upwind integration algorithm, which require either 6– or 12–solutions of the Riemann problem, per cell, per time-step.

Riemann Problem and Riemann Solvers

A Riemann solver is a numerical method used to solve a Riemann problem. It is used in computational fluid dynamics and computational magnetohydrodynamics. A Riemann problem, named after Bernhard Riemann, consists of a conservation law together with piecewise constant data, having a single discontinuity. The Riemann problem is very useful for the understanding of hyperbolic partial differential equations, like the Euler equations, because all properties, such as shocks and rarefaction waves, appear as characteristics in the solution. It also gives an exact solution to some complex nonlinear equations, such as the Euler equations. In numerical analysis, Riemann problems appear in a natural way in finite volume methods for the solution of equation of conservation laws, due to the discreteness of the grid. For that reason, it is widely used in computational fluid dynamics and in MHD simulations. In these fields, Riemann problems are calculated using Riemann solvers. Riemann solvers [52] decompose the solution into three domains. The propagation speed is equivalent to the propagation speed of the sound. The fastest characteristic defines the Courant Friedrichs Lewy condition, which sets the restriction for the maximum time step in a computer simulation. Courant Friedrichs Lewy condition is a necessary condition for convergence while solving certain partial differential equations (usually hyperbolic PDEs) numerically. It is not in general a sufficient condition. It arises when explicit

time–marching schemes are used for the numerical solution. The timestep must be less than a certain time in many explicit time–marching computer simulations, otherwise the simulation will produce wildly incorrect results. For example, if a wave is crossing a discrete grid, then the timestep must be less than the time for the wave to travel to adjacent grid points. When the grid point separation is reduced, the upper limit for the time step also decreases.

The Equations of Ideal Magnetohydrodynamics

The equations of ideal magnetohydrodynamics (MHD) can be written in conservative form as

$$\frac{\partial \rho}{\partial t} + \nabla \cdot (\rho \mathbf{v}) = 0 \tag{3.1}$$

$$\frac{\partial \rho \mathbf{v}}{\partial t} + \nabla \cdot (\rho \mathbf{v}\mathbf{v} - \mathbf{B}\mathbf{B}) + \nabla P^* = 0 \tag{3.2}$$

$$\frac{\partial \mathbf{B}}{\partial t} + \nabla \times (\mathbf{B} \times \mathbf{v}) = 0 \tag{3.3}$$

$$\frac{\partial E}{\partial t} + \nabla \cdot ((E + P^*)\mathbf{v} - \mathbf{B}(\mathbf{B} \cdot \mathbf{v})) = 0 \tag{3.4}$$

where ρ is the mass density, $\rho\mathbf{v}$ the momentum density, $\mathbf{B}$ the magnetic field, and E the total energy density. The total pressure $P^* \equiv P + (\mathbf{B} \cdot \mathbf{B})/2$ where P is the gas pressure. This system of equations is closed with the addition of an equation of state which relates the pressure and density to the internal energy, $\epsilon \equiv E - \rho(\mathbf{v} \cdot \mathbf{v})/2 - (\mathbf{B} \cdot \mathbf{B})/2$.

For the Athena code, an ideal gas equation of state $P = (\gamma - 1)\epsilon$ is assumed, where γ is the ratio of specific heats. The system of units is chosen in which the magnetic permeability $\mu = 1$.

In addition to the evolutionary conservation laws (equations above), the magnetic field must also obey the divergence free constraint, i.e. $\nabla \cdot \mathbf{B} = 0$.

In Athena, a three dimensional, Cartesian grid is assumed. The standard notation is used where the grid cell (i, j, k) is centered at (x_i, y_j, z_k) and has a size $(\delta x, \delta y, \delta z)$. Time levels are denoted by a superscript, and interface values are denoted by half increments to the index, the volume averaged x-component of the magnetic field at time t^n is defined to be $\mathrm{B}^n_{x,i,j,k} \equiv \frac{1}{2}\left(B^n_{x,i-1/2,j,k} + B^n_{x,i+1/2,j,k}\right)$.

The Interface States

For the calculation of the "interface states" the Piecewise Parabolic Method (PPM) algorithm is used for ideal MHD in three dimensions. The PPM interface state algorithm is based upon the idea of dimensional splitting, and, as a result, is a one–dimensional algorithm, including both spatial reconstruction and a characteristic evolution of the linearized system in primitive variables. It is necessary to include multidimensional terms when calculating the interface states. The three dimensional interface state algorithm is thus a generalization of the two–dimensional algorithm, which for consistency must reduce to the two- and one–dimensional algorithm in the appropriate limits. The interface states in the PPM algorithm are typically calculated by evolving the system of equations in primitive variables. For example, the induction equation in component form is:

$$\frac{\partial B_x}{\partial t} + \frac{\partial}{\partial y}\left(v_y B_x - B_y v_x\right) + \frac{\partial}{\partial z}\left(v_z B_x - B_z v_x\right) = 0 \tag{3.5}$$

$$\frac{\partial B_y}{\partial t} + \frac{\partial}{\partial x}\left(v_x B_y - B_x v_y\right) + \frac{\partial}{\partial z}\left(v_z B_y - B_z v_y\right) = 0 \tag{3.6}$$

$$\frac{\partial B_z}{\partial t} + \frac{\partial}{\partial x}\left(v_x B_z - B_x v_z\right) + \frac{\partial}{\partial y}\left(v_y B_z - B_y v_z\right) = 0 \ . \tag{3.7}$$

Instead of proceeding to the details of the three–dimensional algorithm, for simplicity of illustration, the two–dimensional case where equations are linearized is presented. For the two–dimensional (x, y)-case, the induction equation for B_z is sim-

plified using the $\nabla \cdot \mathbf{B} = 0$ condition eliminating the MHD source terms from the evolutionary equation for B_z. The result is the following set of equations for calculating the x-interface states in 2D

$$\frac{\partial B_x}{\partial t} = 0 \tag{3.8}$$

$$\frac{\partial B_y}{\partial t} + \frac{\partial}{\partial x}\left(v_x B_y - B_x v_y\right) = 0 \tag{3.9}$$

$$\frac{\partial B_z}{\partial t} + \frac{\partial}{\partial x}\left(v_x B_z\right) - B_x \frac{\partial v_z}{\partial x} = 0 \ . \tag{3.10}$$

which can, after detailed mathematical analysis, be simpified to the form:

$$\frac{\partial B_x}{\partial t} = 0 \tag{3.11}$$

$$\frac{\partial B_y}{\partial t} + \frac{\partial}{\partial x}\left(v_x B_y\right) - B_x \frac{\partial v_y}{\partial x} - v_y \text{minmod}(\frac{\partial B_x}{\partial x}, -\frac{\partial B_y}{\partial y}) = 0 \tag{3.12}$$

$$\frac{\partial B_z}{\partial t} + \frac{\partial}{\partial x}\left(v_x B_z\right) - B_x \frac{\partial v_z}{\partial x} - v_z \text{minmod}(\frac{\partial B_x}{\partial x}, -\frac{\partial B_z}{\partial z}) = 0 \tag{3.13}$$

where the minmod function is defined as

$$\text{minmod}\left(x, y\right) = \begin{cases} (x)\min(|x|, |y|) & \text{if } xy > 0 \\ 0 & \text{otherwise.} \end{cases} \tag{3.14}$$

The content of this and the previous section was mainly taken from [49] .

Extrasolar Planets Winds

The recent Kepler mission [54] discovered numerous extrasolar planets. Due to observational issues and methods used, the majority of detected planets are relatively close to the parent stars. According to the analysis of the first four months of data [55] ,roughly about fifty percent of those detected planets have an orbit with a semi–major axis less than 0.1 AU. In such circumstances, strong radiation from the star, especially extreme ultraviolet radiation, can heat up the atmosphere of the planet and possibly drive a wind (Moutou et al 2002) [56] . On some planets the extended envelope beyond the Roche lobe of the planet has been directly observed (Vidal–Madjar et al. 2008 ; Ehrenreich 2008) [57] [58] (based on the stellar Lyα flux absorbed by HD209458b). The limit on the mass–loss rate, which was previously observationally constrained for such planets to be larger than 10^{10} g s^{-1} , has recently been refined. The findings of Echenreich & Desert (2011) [59] had put the constraints on the mass–loss rates of all detected transiting planets to be within 10^{6} to 10^{13} g s^{-1}.

The first step on the way to reaching the goal of this project was to reproduce the results of Stone and Proga (2009) [53] , where the extrasolar planet is examined. The planet is located in the vicinity of the star, so the strong wind from the star is present, colliding with the planet wind. The paper examines the influence of the star wind on the total mass–loss rate of the planet. The simulation in their paper is 2.5 dimensional, and therefore cannot include the Coriolis force. In order to secure accuracy and reliability of the results we were testing, the simulation was tested extensively at every stage of development. The project was divided into three steps. The first step created a spherically symmetrical planet, having an interior of constant density and temperature. Such a planet, due to its constant surface temperature and density, creates a spherically symmetric wind. This is, in essence, the Parker problem (Parker, 1965) [61] , which does have an analytical solution. The second step added

the wind from one side, which was put in by hand as a boundary condition for the velocity at the one side of the box (computational domain). The final step added the Coriolis force into the code. This last step was possible due to the fact that the Athena is an open code, and the authors anticipated the eventual need for adding extra physics. Therefore, extra forces can be added to the source code. Figure 11 is an artist rendering of extrasolar planet.

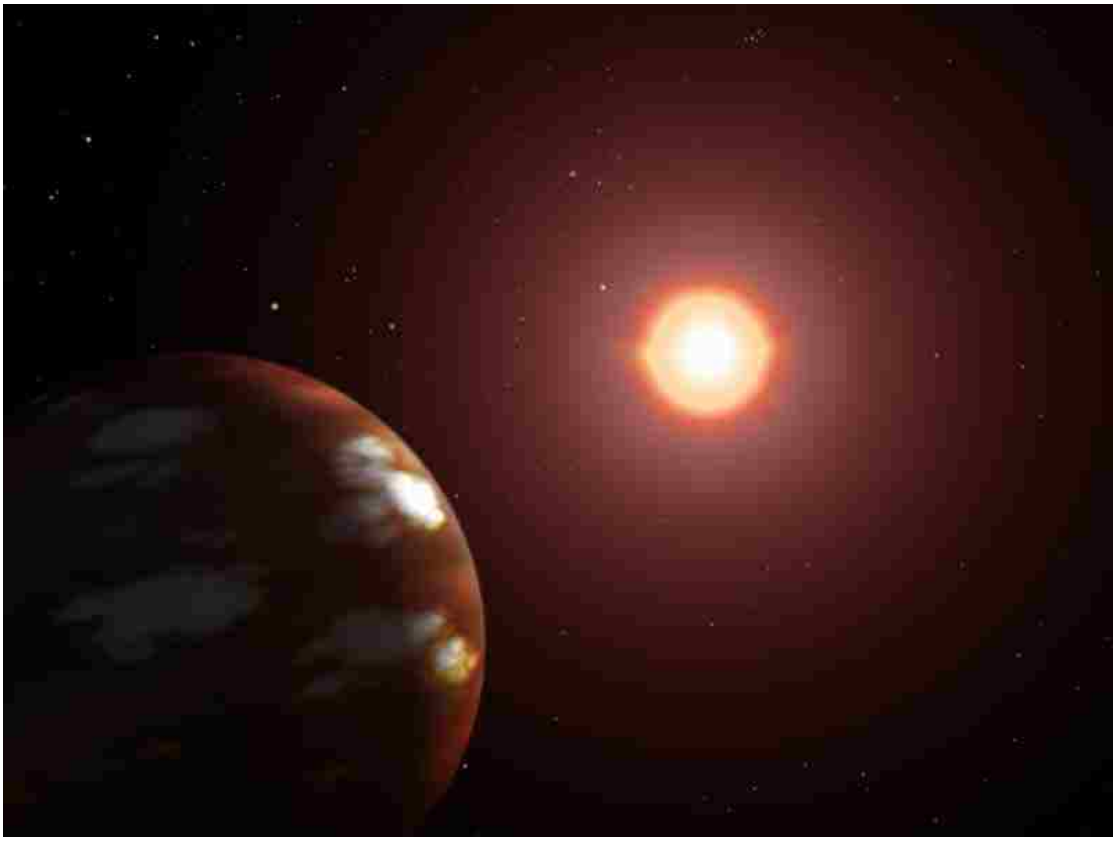

Figure 11 Extrasolar planet (Artist Rendering), http://www.nasa.gov/images

Spherically Symmetric Wind

We performed a nonisothermal simulation, spherically symmetric, with $\gamma = 1.01$, and hydrodynamical escape parameter (HEP) λ, being equal to 5.0. The HEP, is defined as:

$$\lambda = \frac{GM_p\mu}{R_p kT} \tag{3.15}$$

where M_p and R_p are the mass and radius of the planet, and T and μ are the temperature and mean mass per particle in the atmosphere. Numerical values of HEP were previously analyzed by Hunten (1982) [60] , while for λ closer to 10.0, the stronger thermally driven wind will appear. We were running the code for more than a few sound crossing times, so it would reach a steady state. Boundary conditions were set to outflow, and only the central spherical region inside the planet was controlled during the simulation. The spherical zone of $R \leq 1.0$ had a controlled density of 1.0 and the temperature was set to be constant on its surface. In the first step, we numerically solved the exact equation for Parker wind (Parker, 1965) [61] , but since the equation is for the isothermal case, there was a slight mismatch when we compared theoretical results to the results of the simulation. After that, we compared the general γ analytic solution (Holzer & Axford 1970) [62] , for the nonisothermal wind ($\gamma = 1.01$). The figure 12 shows all three : Parker solution for isothermal case ($\gamma = 1.00$), which slightly differs from Holzers & Axfords nonisothermal solution ($\gamma = 1.01$), as well as the solution from the simulation result. The simulation result coincides almost perfectly with the theoretical solution, as can be seen on the graph, figure 12 .

The detailed resolution study was done on the various resolutions: 64, 128, 256 and 512 grid points per dimension. We found that the 256^3 case had errors less than 0.2%, and that the 512^3 case had errors less than 0.1%, with respect to the theoretical exact solution of the Parker wind problem. As far as the resolution is concerned, the experimentalist needs to determine the functional dependence of the resolution vs. the error (compared to the theoretical solution), both the average error over all grid points and the biggest error over the grid points. When the increase of the resolution

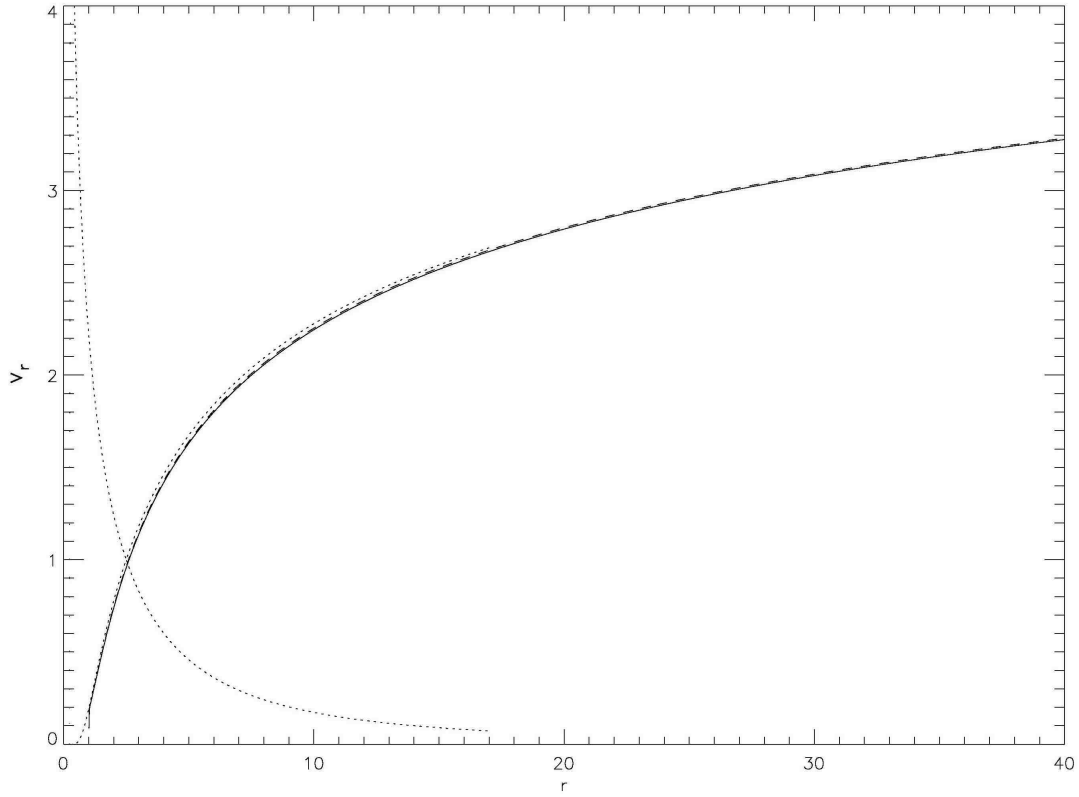

Figure 12 Velocity vs. radius. Dotted line: theoretical Parker solution for isothermal case ($\gamma = 1.$); Solid line: theoretical solution for nonisothermal case ($\gamma = 1.01$); and dashed line: simulation result for nonisothermal case ($\gamma = 1.01$)

starts to negligibly decrease the error and saturate, or if the error falls below a certain percentage value, which is set by the physical limitations of the model, the resolution should not be further increased, since it will only lead to waste of the CPU (and the real) time and be of no benefit at all. Such an approach is necessary while performing the numerical experiment, since one has to know the limitations and the precision of the code which was being used. Of course, the main purpose of numerical experiments is to research problems that are beyond the analytical horizon. The major issue is that before leaving very well–tested grounds, all details about behavior of the model must be taken into account. For that reason, it is a common practice, before attacking

new complex problems, that the model and the code both be tested on problems with existing analytical solutions. For that reason, we did extensive testing on spherically symmetric configurations before making a step toward more realistic non–symmetric problems of extrasolar planets.

The issue with increasing the accuracy of the model, via increasing the resolution, is that doubling the resolution results in an increase of the calculation time by more than a factor of eight. That is due to the fact that the runs are three–dimensional, and such runs very soon become computationally "expensive". The same holds for doubling the size of the domain. We were using clusters of 64 processors for our runs. With that computational power, the 512^3 was the highest resolution we were running, due the time limitations imposed. Particularly for runs like this, on a 64 processor cluster, the system reaches the steady state in between 50 and 100 units of computational time, which corresponds roughly to one week of real time.

Cosine Distribution of Temperature Introduced

The geometry of the system dictates that the temperature of the surface of the planet is dependent upon the latitude, and therefore the cosine–like distribution of the temperature on its surface is natural. Because of the minimal energy configuration, most of the close–in EGPs are tidally locked, so the only mechanisms that can transport heat to the "night" side are bulk flows in the atmosphere and thermal conduction. After testing for a spherically symmetric case, we continued simulations: introducing the cosine temperature distribution, keeping the surface of the planet on the "night" side on a very small temperature of (0.01% of the "day" side maximum), while controlling the "day" side temperature as a cosine function of θ angle with the respect to the star, and the wind from the star, which is not introduced yet at this stage, figure 3 and figure 14.

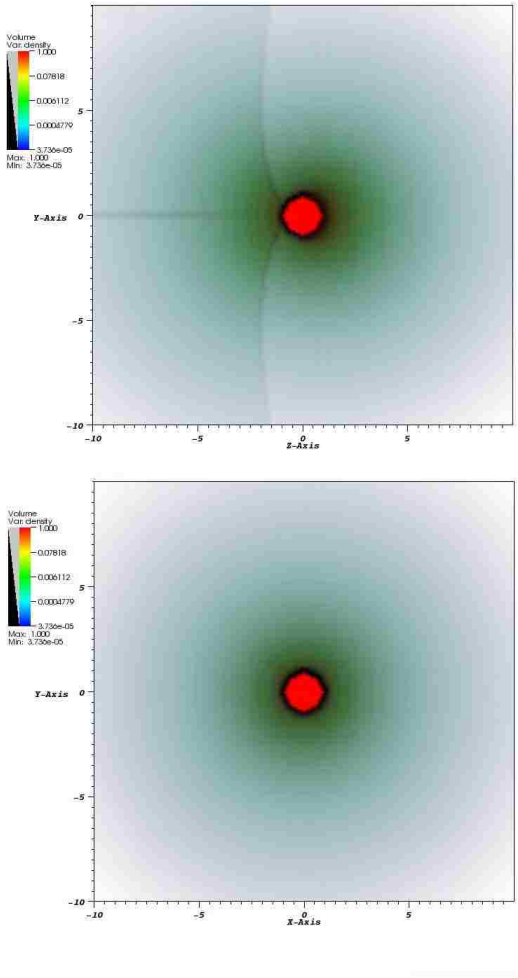

Figure 13 3D cut at y=0 (top panel), and z=0 (bottom panel) for the run with the cosine heating included

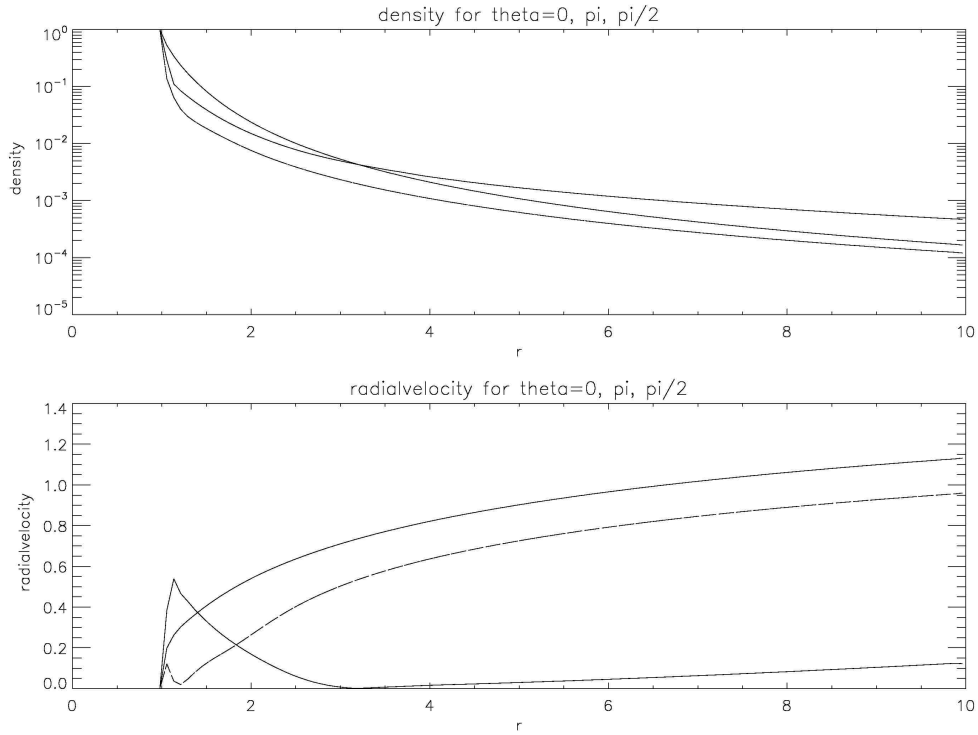

Figure 14 Plot of density and velocity along radial lines, for the run with cosine heating included, $\theta = 0$ (solid), $\theta = \pi/2$ (dashed) and $\theta = \pi$ (dotted)

Introducing the Stellar Wind

By including the stellar wind in the domain at one side of the box, the same side from which the radiation is hitting the planet, we effectively repeated the work of Stone and Proga only in 3D [53] , where one can see that the approximation of axial symmetry they had is more than justified. However, this still does not fully reproduce the realistic model, since the planet is rotating around the parent star. Because the star in reality does rotate, the Coriolis force is present, as well as the effects of the star moving through the medium.

Table 2 Summary of the extrasolar planets results

No. of run	λ	GM	R_{domain}	Ω_{planet}	$v_{star\ wind}$	$\rho_{star\ wind}$	$v_{max\ (planet\ wind)}$	$\dot{M}_{planet}$
W9	5.0	1.0	20.0	0.0	1.0	10^{-3}	2.77	4.75
W13	5.0	1.0	20.0	0.0	4.0	10^{-3}	4.11	3.08
W22	5.0	1.0	20.0	0.0	0.25	10^{-4}	1.63	6.04
C10	5.0	1.0	20.0	5.0	0.25	10^{-4}	1.59	6.04
C15	5.0	1.0	20.0	0.5	0.25	$0.5\,10^{-4}$	2.06	6.18
C19	5.0	1.0	20.0	5.0	0.5	$0.5\,10^{-4}$	4.68	2.31

* All quantities expressed in this table are unitless

In this part of the research, we put an emphasis on the geometry of the wind. The strength of the wind controls the mass–loss rate, and the mass–loss rate will obviously control the lifetime of the planet. The high temperatures cause the planet's atmosphere to extend outside of the Roche lobe, and, therefore, the estimates on the lifetime can be calculated, dependent upon the predicted mass–loss rate and the mass of the planet. Many theoretical mechanisms have been proposed to explain various physical causes for the evaporation of the planet (Fortney & Nettelmann,2010) [63] , but the heating caused by the parent star and the interaction with its wind seem to be the most relevant ones. Here we present the results of different models with similar structures and different parameters, and the simulation results for the mass–loss rate in dimensionless units, as shown in figure 3 and in the table 2 . In the figure, the line of shock where the star's wind is colliding with the outflow wind from the planet is clearly visible on the upper side (in a parabolic shape), while two shocks on the left and right sides, created by the planet outflow itself, are still present and visible on the figure 3 . A strong stellar wind confines the planetary wind to a small volume and enhances the column density close to the planet.

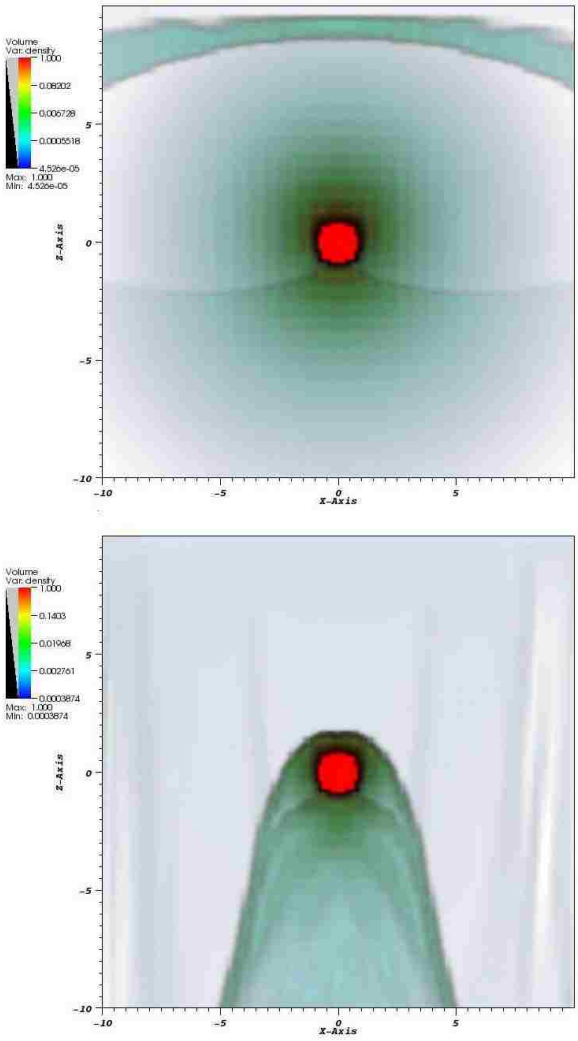

Figure 15 3D cut at y=0, runs "W22" (top panel) and "W13" (bottom panel) with the star wind included, the two represent relatively weak and very strong wind coming from the positive z direction, having negative z velocity component

Introducing Coriolis Force

The Coriolis force is given by the formula:

$$F_C = 2\,m\,\Omega \times v \tag{3.16}$$

In the model we are presenting, the wind coming from the star enters the computational domain from the positive z side, and has negative z velocity. Its velocity and momentum are controlled by the boundary condition introduced. This geometry has the star on the z axis of the computational domain, located very high on the positive z side. Therefore, the choice of the orientation of the vector of the planet's rotational velocity is arbitrary within the x–z plane of the computational domain, and we have chosen the direction y for the Ω_{planet}. Therefore, the above vector product results in the following acceleration present within the system:

$$a_{coriolis} = 2\,\Omega_{planet}\,(\hat{x}v_z - \hat{z}v_x) \tag{3.17}$$

We varied the rotational velocity, or the period of the planet orbiting the star, by adjusting Ω_{planet} in the part of the code which we have written to include this effect. The resulting mass loss quantities are listed in the table 2 in a few bottom rows. Since the hundreds of planets recently discovered by the Kepler mission [55] have a wide variety of periods, by changing the rotational velocity of the whole domain around the star, we tested the model for sensitivity on Coriolis effect. Our findings are that mass–loss rate is almost not at all influenced by Coriolis force in the models we exploited. However, if the rotation velocity gets very large (period of a planet gets very small) then the Coriolis force might be larger than a 1% importance. But such a scenario can also cause some further numerical complications, with respect to smaller scale shocks occurring throughout the domain.

On the other hand, the geometry of the flow is heavily influenced by the Coriolis force, and any symmetry is immediately broken as soon as the Coriolis force kicks into the system. As can be seen on figure 16 , the geometry is changed due to the combined influences of the Coriolis force and the strength of the wind around the planet. On the top panel, the run "C10" shows small but clearly visible deviations from the axial symmetry. On the bottom panel, the run "C19" is shown, and the strength of the effect is overwhelming and very close to breaking the dynamic equilibrium of the planet's wind.

The figure 17 shows plots of density and total velocity for the run "C19" at the constant radii: 2.0, 5.0, and 10.0. On this graph, it is visible that a small vorticity over the whole domain is introduced. At this strength, it is just slightly influencing the geometry of the wind, leaving the wind at the stable dynamical equilibrium.

On the figure 16 it can be seen that there are two slightly curved shocks present, extending in positive and negative x direction from the planet. Those two shocks are visible on the figure too, only in the case without the Coriolis force, the curvature of the shock line is the consequence of the heating on the "day" side of the planet. In this case, the shock is created by the angular motion of the atmosphere caused by differences in the temperature. Same shock first, when wind from the star is added, as can be seen on figure gets slightly dislocated in negative z direction for the case of the weak wind, the shock line gets strongly dislocated in case of the strong wind. In cases before introduction of the Coriolis force the system is still axially symmetric, and the introduction of the Coriolis force breaks the symmetry and adds vorticity in the system, by displacing the shocks in angular direction as shown on the figure 16 .

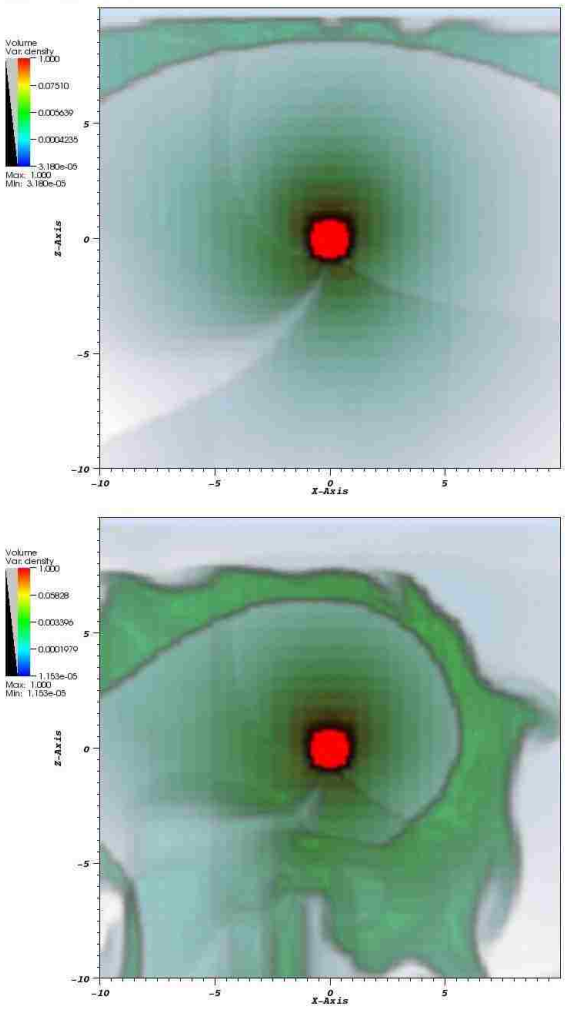

Figure 16 3D cut at y=0, runs "C10" (top panel) and "C19" (bottom panel) with the star wind and the Coriolis force included, the two represent a relatively weak, and a very strong, Coriolis Force influencing the geometry of the flow.

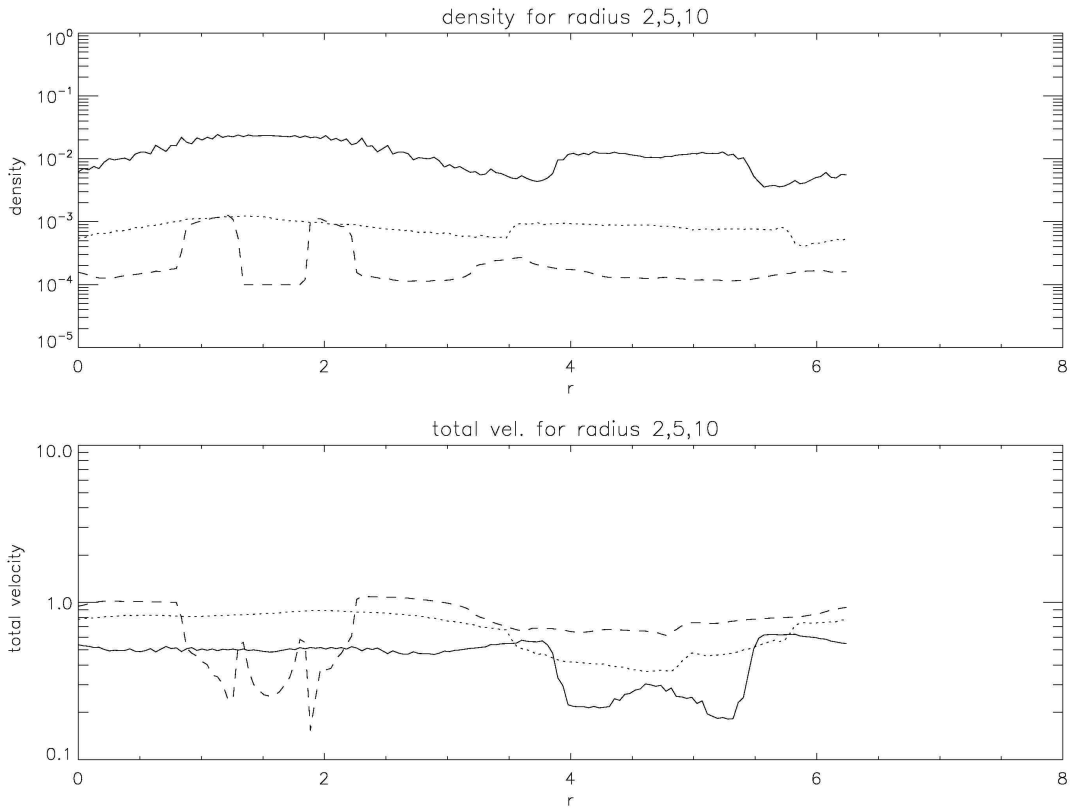

Figure 17 run: "C10" Plots of density and total velocity along the equidistant lines for radiii: 2 (solid), 5 (dotted) and 10 (dashed)

Conclusion

Mass losses in the simulations with the Coriolis force included varied for less than 1% and all mass losses, in all runs, varied within a range of a factor of two. When such a model is applied to the realistic case, it can give an estimate of the life length of a planet in a similar environment. To our knowledge, no similar simulations of extrasolar planets in 3D with Coriolis force included have been done to date. There have been simulations where the Athena code was used and the Coriolis force was included (Lemaster et. al, 2007) [64] , but on a different problem. The predictions provided by this model can in the future easily be used for putting constraints on

mass losses of specific extrasolar planets recently discovered by the Kepler mission. Also, the model can be refined by the simple increase of the resolution and increase of the size of the computational domain. The problem we were facing was that in addition to the number of runs with different parameters in the first part (accretion disk problem) compared to this one, the 3D simulations are extremely time (and CPU) consuming. We used a cluster of 64 processors and used the parallelized code. With the size cluster we were using, the average simulation with 256^3 grid points took a couple of days, while the 512^3 one took about two weeks.

CHAPTER 4

CONCLUDING REMARKS

Universal approach to different problems with different geometries

We presented numerical simulations of accretion disks and extrasolar planets, problems that have different geometries, using different softwares but still methodically using the common approach to both problems from the physical point of view. Essentially, our model introduces the surface, in some cases flat, in some cases curved, with controlled distribution of density and temperature, and other parameters. Such surface then affects the rest of the computational domain, and without any "by hand" interventions in the rest of the domain (except for defining the equation of state) can reproduce the evolution of physically very distinct astrophysical problems. The results are showing that this approach may illuminate many aspects of the analyzed problems, like the geometries of the flows with different parameters, and can certainly provide numerical constraints on physical quantities, such as mass–loss rate, density, velocity, and the temperature of the outflows, as well as the detailed geometry of the outflow and others. In the first part, we clarified the mechanism that drives the wind in GRO J1655-40, while in the second part we created firm grounds for studying many newly discovered extrasolar planets and their atmospheres by the recent Kepler mission.

Our approach to the apparently different problems throws light on the method of numerical simulation itself. It shows how two problems, which from the experimental and even theoretical point of view, may have very little in common, may fall into two separate categories or fields of research, when analyzed via numerical simulation or a "numerical experiment", and may be "unified" into a single problem or setup. More precisely, this could be described with the same numerical model, where only the parameters, geometry, boundary, and initial conditions are changed. This clearly

illustrates the nature and uniqueness of this numerical approach as being distinct from experimental and theoretical, though somehow unifying them. It also emphasizes that this very way of analyzing the problem, in certain circumstances, may be capable of providing deeper insight into problems which would, without it, be considered mutually non–related.

REFERENCES

[1] Woods, D.T., Klein, R.I., Castor, J.I., & McKee, C.F. 1996, ApJ, 461, 767

[2] Begelman, M.C., McKee, C.F., & Shields, G.A. 1983, ApJ, 271, 70

[3] Shields, G.A., McKee, C.F., Lin, D.N.C., & Begelman M.C. 1986, ApJ, 306, 90

[4] D., & Kallman, T. 2002, ApJ, 565, 455 (PK02)

[5] D. , Stone, J., & Kallman, T. 2000, ApJ, 543, 686

[6] Stone, J.M., & Norman, M.L. 1992, ApJ Suppl., 80, 753

[7] Miller, J. M., Raymond, J., Fabian, A. C., Steeghs, D., Homan, J., Reynolds, C.S., van der Klis, M., & Wijnands, R. 2006, Nature, 441, 953 (M06)

[8] Proga, D. 2006, Nature, 441, 938

[9] Netzer, H. 2006, ApJ, 652, L117 (N06)

[10] Miller, J.M., Raymond, J., Reynolds, C.S., Fabian, A.C., Kallman, T.R. , & Homan, J. 2008, ApJ, 680, 1359

[11] Schneider, J., 2011, http://exoplanet.eu/catalog.php

[12] Mayor, M., Bouchy, F., Benz, W., Lovis, Ch., Mordasini, Ch., Pepe, F., Queloz, D.,Udry S. (2008) Below 25 Earth-masses: A specific planetary population. In Extrasolar Super-Earths. University of Nantes, France, 16. 18. June 2008.

[13] Schneider, J., Boccaletti, A., Mawet, D., Baudoz, P., Beuzit, J.-L., Doyon, R., Marley, M., Stam, D., Tinetti, G. Traub, W., Trauger, J., Aylward, A., Cho ,J. Y-K., Keller, C.-U., Udry, S., and the SEE-COAST TEAM. (2009) The Super Earth Explorer: A coronagraphic off-axis space telescope. Exp. Astron. 23:357-377

[14] Cockel, C. S., Herbst, T., Lger, A., Absil, O., Beichman, C., Benz, W., Brack, A., C., Chelli, A., Cottin, H., Coud du Foresto, V., Danchi, W., Defrre, D., den Herder, J.-W., Eiroa, C., Fridlund, M., Henning, Th., Johnston, K., Kaltenegger, L., Labadie, L., Lammer, H., Launhardt, R., Lawson, P., Lay, O. P., Liseau, R., Martin, S. R., Mawet, D., Mourard, D., Moutou, C., Mugnier, L., Paresce, F., Quirrenbach, A., Rabbia, Y., Rottgering, H. J. A., Rouan, D., Santos, N., Selsis, F., Serabyn, E., Westall, F., White, G., Ollivier, M., Bord, B. (2009) Darwinian experimental astronomy mission to search for extrasolar planets. Exp. Astron. 23:435-461

[15] Lawson, P., Lay, O., Martin, S., Peters, R., Gappinger, R., Ksendzov, A., Scharf, D., Booth, A., Beichman, C., Serabyn, E., Johnston, K. and Danchi, W. (2008) Terrestrial Planet Finder Interferometer: 2007-2008 progress and plans. In Proceedings of the SPIE, 7013:70132N- 70132N-15.

[16] Glassman, T., Newhart, L., Barber, G., Turnbull, M. and NWO Study Team. (2009) Planning an efficient search for extra-solar terrestrial planets: How To Find Exo-Earths with New World Observer. In American Astronomical Society (AAS) Meeting 213, 404.04

[17] Shaklan, S., Levine, M., Proceedings of the conference In the Spirit of Bernard Lyot: The Direct Detection of Planets and Circumstellar Disks in the 21st Century. June 04 - 08, 2007. University of California, Berkeley, CA, USA.

[18] Koechlin L., Serre D., Debra P., Pella R., Peillon Ch., Duchon P., Gomez de Castro A., Karovska A., Desert J.-M., Ehrenreich D., Hebrard G., Lecavelier des Etangs A., Ferlet R., Sing D., Vidal-Madjar A., 2009, Exp. Astron., 23:379-402.

[19] Lillie, C. (2001) TRW TPF Architecture. Phase 1 Study, Phase 2 Final Report. http://planetquest.jpl.nasa.gov/TPF/TPFrevue/FinlReps/Trw/TRW12Fnl.pdf.

[20] Seager, S. & Deming, D. 2010, Annu. Rev. Astron. Astrophys., 48:63172

[21] Hubbard, W.B., Hattori, M.F., Burrows, A., Hubeny, I., & Sudarsky, D., 2007. Icarus, 187, 358.

[22] Lecavelier des Etangs, A., 2007. A&A 461, 1185.

[23] Colella P., & Woodward, P. R., 1984, J. Comp. Phys., 54, 174

[24] Oran, E. S., &8 Boris J. P., 1987, Numerical Simulation of Reactive Flow, Elsevier: New York

[25] Sod, G. A., 1985, Numerical Methods in Fluid Dynamics, Cambridge University Press: Cambridge: p. 179.

[26] von Neumann, J., & Richtmyer, R. D. 1950, J. Appl. Phys., 21, 232

[27] The Zeus–2D Code for Astrophysical Fluid Dynamics Simulations, 1992

[28] Williams, J., P. & Cleza, L., A. 2011, Annual Review of Astronomy and Astrophysics Vol. 49

[29] Font, A. S., McCarthy, I. G., Johnstone, D., Ballantyne, D. R., 2004, ApJ, 890, 607

[30] Luketic, S., Proga, D., Kallman, T. R., Raymond, J. C., Miller, J. M. 2009, Apj, 719, 515 (Reproduced by permission of the AAS)

[31] Miller, J. M., Raymond, J., Homan, J., Fabian, A. C., Steeghs, D., Wijnands, R., Rupen, M., Charles, P., van der Klis, M., & Lewin, W. H. G. 2006, ApJ, 646, 394

[32] Orosz, J.A., & Bailyn, C.D. 1997, ApJ, 477, 876

[33] Kubota, A., Dotani, T., Cottam, J., Kotani, T., Done, C., Ueda, Y., Fabian, A. C., Yasuda, T., Takahashi, H., Fukazawa, Y., Yamaoka, K.,; Makishima, K., Yamada, S., Kohmura, T., & Angelini, L. 2007, PASJ, 59S, 185

[34] Neilsen, J., & Lee, J.C. 2009, Nature, 458, 481

[35] Shulz, N.S., & Brandt, W.N. 2002, ApJ, 572, 971

[36] Blandford, R.D., & Payne, D.G. 1982, MNRAS, 199, 883

[37] Balbus A., & Hawley J.F. 1998, Rev. Mod. Phys. 70, 153

[38] Proga, D. 2006, Nature, 441, 938

[39] Kallman, T. R., Bautista, M.A., Goriely, S., Mendoza C., Miller, J.M., Palmeri, P., Quinet, P., & Raymond, J. 2009, ApJ, 701, 86

[40] Proga, D., Stone J.M., & Drew J.E. 1998, MNRAS, 295, 595

[41] Kallman, T. R., & Bautista, M. 2001, ApJS, 133, 221

[42] Bautista, M., & Kallman, T. 2001, ApJS, 134, 139

[43] Dorodnitsyn, A., Kallman, T., & Proga, D. 2008, ApJ, 687, 97

[44] Jimenez-Garate, M.A., Raymond, J. C., & Liedahl, D.A. 2002, ApJ, 581, 1297

[45] Jimenez-Garate, M.A., Raymond, J.C., Liedahl, D.A., Hailey, C.J. 2005, ApJ, 625, 931

[46] Miller, J. M., Raymond, J., Homan, J., Fabian, A. C., Steeghs, D., Wijnands, R., Rupen, M., Charles, P., van der Klis, M., & Lewin, W. H. G. 2006, ApJ, 646, 394

[47] Godunov, S. K. (1959), "A Difference Scheme for Numerical Solution of Discontinuous Solution of Hydrodynamic Equations", Math. Sbornik, 47, 271306, translated US Joint Publ. Res. Service, JPRS 7226, 1969.

[48] Einfeldt, B. (1988), "On Godunov-type methods for gas dynamics", SIAM J. Numer. Anal. 25: 294318

[49] T.A. Gardiner & J.M. Stone, 2005, J. Comput. Phys. 205, 509

[50] T.A. Gardiner & J.M. Stone, 2007, JCP, 227, 4123

[51] P. Colella, 1990, J. Comput. Phys. 87, p. 171.

[52] Toro, Eleuterio F. (1999). Riemann Solvers and Numerical Methods for Fluid Dynamics. Berlin: Springer Verlag. ISBN 3-540-65966-8.

[53] Stone, J.M., Proga, D., 2009, ApJ, 694, 205S

[54] http://kepler.nasa.gov/

[55] W. J. Borucki et al. Characteristics of planetary candidates observed by Kepler, II: Analysis of the first four months of data, 2011

[56] Moutou C. et al. 2001, AA, 371, 260

[57] Vidal–Madjar, A. et al 2008,ApJ, 676, L57

[58] Ehrenreich, D. et al.,2008, AA, 483, 933

[59] Ehrenreich, D. & Desert, J.–M.,2011, arXiv: 1103.0011v1

[60] Hunten, D.M. 1982. P&SS, 30, 773

[61] Parker, E. N., 1965, Fermi Insitute, University of Chicago

[62] Holzer, T., E. & Axford W.I. 1970, Rev. Astron. Astrophys. 8, 31

[63] Fortney, J.,J, & Nettelmann N. 2010, Space Sci. Rev., 152, 423

[64] Lemaster, M., N., Stone, J., M. & Gardiner, T., A. 2007, ApJ, 662, 582

VITA

Graduate College
University of Nevada, Las Vegas

Stefan Luketic

Degrees:

Bachelor of Physics, 2002, Master of Physics, 2007
Univeristy of Zagreb, Faculty of Science, Department of Physics

Publications:

Luketic, S.; Proga, D.; Kallman, T. R.; Raymond, J. C.; Miller, J. M., *On the Properties of Thermal Disk Winds in X-ray Transient Sources: A Case Study of GRO J1655-40*, 2010, ApJ, 719, 515

Luketic, S.; Proga, D., in preparation in preparation

Giustini, M., Proga, D., Luketic, S., tentative title: "Line Profiles From Disk Winds – Effects of Magnetic Fields, Radiation Pressure and Gas Pressure", in preparation

Dissertation Examination Committee:

Chairperson, Daniel Proga, PhD
Committee Member, Stephen Lepp, PhD
Committee Member, Michael Pravica, PhD
Graduate Faculty Representative, Rohan Dalpatadu, PhD